Late Cenozoic evolution of the Ariège River valley (Pyrenees) constrained by cosmogenic 26Al/10Be and 10Be/21Ne dating of cave sediments

Amandine Sartégou, Pierre-henri Blard, Regis Braucher, Didier Bourlès, Patrick Sorriaux, Laurent Zimmermann, Alexis Laffitte, Bouchaïb Tibari, Laëtitia Leanni, Valéry Guillou, et al.

Late Cenozoic evolution of the Ariège River valley (Pyrenees) constrained by cosmogenic $^{26}Al/^{10}Be$ and $^{10}Be/^{21}Ne$ dating of cave sediments

Amandine Sartégou *(1,2), Pierre-Henri Blard (3,4), Régis Braucher (2), Didier L. Bourlès (2), Patrick Sorriaux (5), Laurent Zimmermann (3), Alexis Laffitte (6), Bouchaïb Tibari (3), Laëtitia Leanni (2), Valéry Guillou (2), ASTER Team[+] (2) and Audry Bourdet (1)

(1) Université de Perpignan–Via Domitia, CNRS UMR 7194 Histoire Naturelle de l'Homme Préhistorique, 52 avenue Paul Alduy, F-66860 Perpignan Cedex, France ; (2) Aix-Marseille Univ., CNRS-IRD-Collège de France-INRAE, UM 34 CEREGE, Technopôle de l'Environnement Arbois-Méditerranée, BP80, 13545 Aix-en-Provence, France ; (3) CRPG, UMR 7358, CNRS-Université de Lorraine, 15 rue Notre-Dame des Pauvres, 54501 Vandœuvre-lès-Nancy, France ; (4) Laboratoire de Glaciologie, ULB, Bruxelles, (5) Route de Surba, 09400 Bédeilhac, France; (6) Université de Toulouse, UPS (OMP), GET, Toulouse, France

[+] *Georges Aumaître, Karim Keddadouche*

**corresponding author; E-mail address: sartegou@cerege.fr / amandine.sartegou@gmail.com (A. Sartégou)*

Abstract

Despite increasing knowledge on the orogenic phases of the Pyrenees, the Neogene evolution of the range remains poorly constrained. The central Pyrenees, particularly the Ariège River valley and its terrace systems and glacial extensions, are key to reconstructing Pyrenean evolution during the Neogene. However, few terrace relics remain on the piedmont edges. To overcome this limitation and temporally extend the dataset obtained from terraces, we focus on alluvium-filled horizontal epiphreatic passages developed in limestone karstic networks. These landforms record the transient position of former local base levels during the process of valley deepening, similar to fluvial terraces. The alluvium fills of the studied caves in the Tarascon-sur-Ariège area, in the transition zone between the upper range and the piedmont, therefore enable the reconstruction of the geodynamic evolution of the Ariège River valley. All studied caves are developed on at least eight levels. Based on burial durations determined by $^{26}Al/^{10}Be$ and $^{10}Be/^{21}Ne$ terrestrial cosmogenic nuclide dating of

samples from epiphreatic levels, our results indicate Langhian to Messinian (~13–5 Ma) incision rates averaging 48 m Myr^{-1}. However, the obtained record does not allow us to accurately retrace the Pliocene evolution of the area due to the lack of known caves at corresponding levels. Moreover, raised local base levels during glacial phases both make the record more complex and call into question the methodological approach in terms of potential internal sediment remobilization and mixing related to implied re-flooding periods.

Keywords

Cave deposits, cosmogenic burial dating, ^{26}Al, ^{10}Be, ^{21}Ne, incision rates, Pyrenees, karst geomorphology.

Highlights

- We identify eight regional cave levels in a Neogene valley in the eastern Pyrenees
- $^{26}Al/^{10}Be$, $^{10}Be/^{21}Ne$ burial durations obtained for intrakarstic alluvium
- Langhian-Messinian valley incision rates were ~48 m Myr^{-1}
- Palaeodenudation rates increased by one order of magnitude since the Miocene
- Cave re-flooding events preclude a post-Pliocene reconstruction of the Ariège valley

1- Introduction

Landscapes evolve via interactions between internal and external forcings. Deciphering these retroactions rely on the knowledge of the deformation, exhumation and sedimentation chronologies. The Pyrenees, an intraplate collisional range, were built by the shortening of continental thinned margins during the convergence between Iberia and Eurasia lasting from the Late Cretaceous to the Early Miocene. Because of the duration of the orogenic growth and of its sedimentary evolution that both happen during the Cenozoic climatic cooling, the Pyrenees appear particularly well-suited to investigate coupling and retroactions between climate and tectonics and to attempt quantifying accretion and erosion fluxes. In the case of the Pyrenees, most recent studies have focused on their evolution during Quaternary glaciation phases (e.g., Stange et al., 2013; Delmas et al., 2015; Crest et al., 2017). However, the geomorphological evolution of the Pyrenees during the Neogene is less constrained, and several uplift and incision scenario remain debated (e.g., Babault et al., 2005, Calvet and Gunnell, 2008; Gunnell et al., 2009; Bourdet, 2014; Monod et al., 2016a; Sartégou, 2017; Sartégou et al., 2018). Recent works have focused on incision rates by dating alluvial terraces (e.g., Stange et al., 2012, 2013, 2014; Delmas et al., 2015; Nivière et al.,

2016) and the Lannemezan megafan (Mouchené et al., 2017). However, methodological limitations and the limited preservation of alluvial terraces preclude constraining incision rates prior to the Mio-Pliocene transition. Therefore, the upstream history of valley incisions, particularly those excavated into limestone massifs, may prove useful.

Incision events can be recorded via horizontal karstic systems, and some epiphreatic levels are established in direct relation with their former base levels. Due to variations in these former base levels, such karstic systems are staggered, and the alluvial deposits they record enable the valley incision history to be traced based on their burial duration (e.g., Hauselmann and Granger, 2005; Mocochain et al., 2009; Plan et al., 2009; Sartégou et al., 2018). However, valley evolution is often complex; the Pyrenees have undergone intense glaciation phases that marked the landscape and may have impacted the incision records.

Several studies have focused on the Niaux cave and its surroundings, and the Tarascon-sur-Ariège area (France), has thus become fairly well known. This region is located at the transition zone between the upper Pyrenees and the piedmont. At the surface, the spatial and chronological footprints of six Würmian (MIS 2 to 5) and pre-Würm glaciation stages are constrained by *in-situ* ^{10}Be dating of glacial margin deposits (Delmas, 2009). The stratigraphy and sedimentology of the Niaux cave fills and U-Th dating of several stalagmite floors provide a chronological framework for the last 350 kyr and the first evidence of multiple glaciation cycles in Pyrenean valleys (Sorriaux, 1981, 1982; Bakalowicz et al., 1984). Nevertheless, these data comprise indirect dates for interglacial stalagmite floors, and no study has established a link between the surface sedimentary archives on the slopes of the Ariège River catchment and the intrakarstic deposits.

The aim of this study is to date alluvium injection phases in karstic networks of the Tarascon-sur-Ariège area and estimate the minimum formation age of large phreatic galleries in relation to the floor altitude of neighbouring valleys (Sorriaux et al., 2016). We explored 8 epiphreatic levels in the Ariège River catchment, surveyed 21 horizontal caves, and collected alluvial deposits in 11 caves for cosmogenic nuclide analyses (^{10}Be, ^{26}Al, and/or ^{21}Ne). The limitations of our methodologies and the importance of our selection of dating objects is given particular focus. Notably, the significant influence of cave re-flooding episodes that caused a partial evacuation of the previous sediments within a cavity is investigated. We show that karstic landforms record the history of the Ariège River valley incision, and that the data acquired in this region cannot explain the late Neogene valley via a simple topographic uplift mechanism. The evolution of the palaeodenudation rates, that increased by an order of magnitude between the Miocene and the Quaternary, are also discussed.

2- Geological and geodynamical contexts

2.1- Lithological and structural contexts of the central-eastern Pyrenees

The Pyrenees (southwestern Europe) formed along the boundary between the Iberian and European plates due to the Late Cretaceous-Cenozoic inversion of a Cretaceous transcurrent hyper-extended rift created during the opening of Biscay Bay (e.g., Lagabrielle et al., 2010). This mountain range forms a 400-km-long geographical barrier oriented N110° (e.g., Choukroune, 1992). Pyrenean structures extend along the southern shore of the Biscay Bay to the Asturias Mountains in the west. The Axial Zone of the Pyrenees comprises various terrains of Precambrian and Palaeozoic ages that were folded during the Carboniferous (355–295 Ma) Hercynian orogeny (Engel, 1984).

Figure 1

The source of the Ariège River is Lac Noir (2,400 m above sea level, a.s.l.), in the Font-Nègre cirque. In its upper course, the Ariège River crosses the crystalline Hospitalet massif towards the northeast before its confluence with the Oriège and Lauze rivers. It then flows northwest through the Tabe and Montcalm massifs in the bottom of a glacial trough before reaching Tarascon-sur-Ariège (Fig. 1). The Ariège River receives the waters of several tributaries such as the Najar (confluence at Savignac), Aston (confluence at Les Cabannes), Vicdessos (confluence at Tarascon), and Saurat (confluence at Tarascon), and brings water to crystalline massifs. After its confluence with the Aston, the Ariège River crosses the North Pyrenean fault and incises the strongly deformed and faulted Cretaceous limestone of the North Pyrenean Zone. Beyond Tarascon, the Ariège River flows towards the north, and then enters the Garonne at Portet-sur-Garonne (south of Toulouse), from where it connects to the Atlantic Ocean.

Table 1

The lithostructural framework along the Ariège is complex (see supplementary material for a detailed geological description). The massifs are strongly folded and faulted (Fig. 1). The Ariège river drains quartz-crystalline zones in its southern distal part (in the upper chain) before incising downstream limestone-rich areas in the North-Pyrenean zone, where numerous karsts and caves are developed.

Figure 2

2.2- Quaternary history of the Ariège catchment

During glacial periods, astronomically driven climate fluctuations triggered the development of the Ariège glacier, whose dynamics contributed to downstream valley incision (e.g., Goron, 1937). These events are recorded in the studied caves, through morphologies and sediments. The composite glacier of the Ariège basin was therefore one of the largest Pleistocene glaciers on the northern slope of the Pyrenees. At the maximum of the last glacial period, between 25 and 20 ka, the Ariège glacier reached an altitude of approximately 1,300 m a.s.l. at the confluence with the Aston glacier, implying an ice thickness of 800 m. Only the highest limestone massifs, including those of Quié de Lujat, emerged from this ice surface (Fig. S1, supp. info). Moreover, the ice diffused towards neighbouring valleys on all sides. In the Vicdessos valley, glaciers only reached 1,000 m a.s.l. in the valley of Génat and did not exceed 500 m a.s.l. in the Niaux glacial basin. North of the basin, ice thicknesses exceeded 400 m, implying that the glacier front must have been much further downstream and may have reached the Foix-Montgaillard basin (Delmas, 2009).

3- Karst features and cave systems

We investigated several massifs in the vicinity of Tarascon-sur-Ariège (Fig. 2; Table 1), three of which are karstified (Cap de la Lesse, Sédour, and Calamès). The karst maximum altitude is 1,189 m a.s.l., and the Ariège flows at 470 m a.s.l. at Tarascon. Consequently, in these Cretaceous massifs affected by tight folds and inverse faults (Sorriaux, 1982), nine to ten staggered levels have been identified along nearly 900 m of elevation. Unlike the Têt River valley (Sartégou et al., 2018), karstic levels are vertically connected in some massifs of the Ariège River valley, particularly Cap de la Lesse. Epikarstic morphologies are difficult to study in this area due to the presence of vegetation.

3.1- Cap de la Lesse massif

In the Cap de la Lesse massif, two karstic networks belonging to the large Niaux-Lombrives-Sabart network are notably developed (Fig. 3). Although they are small in extent (5 km²), their accessible gallery network extends more than 14 km. This karst is located between the deep Vicdessos and Ariège valleys (520 and 480 m a.s.l. at their respective valley floors). The upper part comprises the Niaux and Lombrives caves and the upper galleries of the Sabart cave, whilst the lower part includes the lower galleries of the Lombrives cave and

two large halls of the Sabart cave; upper and lower parts are connected by large vertical shafts in Lombrives cave and by two large chimneys that seem to rise towards the Cap de la Lesse summit in the Niaux system (Abîme Martel, 967 m a.s.l., and Salon Noir, 780 m a.s.l.; Fig. 3). The entire Niaux karstic system is currently dry (Sorriaux, 1982) and belongs to the infiltration zone, from which it is fed by seeps only. However, Sorriaux (1982) showed that this karstic system was previously crossed three times by more or less rapid flows, which delivered gneisses and granites from the Pyrenean Axial Zone and North Pyrenean primary massifs. The galleries were therefore repeatedly and sometimes totally filled, then partially to completely emptied (Sorriaux, 1982). Three alluvial formations have been identified by Sorriaux (1982) as: the "alluvial formation of Lombrives" (F1), "conglomerates of the gallery of the Counts of Foix" (F3) and "alluvial formation of Niaux" (F5); site names ‘F-’ refer to the sites where these formations are best represented. The alluvial formation of Niaux exists only throughout the upper stage of the system, whereas the other two are ubiquitous throughout the system. Because these fillings must have been deposited in previously formed galleries, karstogenesis was anterior to the oldest deposits.

The “alluvial formation of Lombrives”, the oldest by relative chronology, was rubified, which produced kaolinite in the east and northeast sections of the karst (Sorriaux, 1982). Because these alluvial sediments were deposited via turbulent currents or debris flows (Sorriaux, 1982), sediment particle sizes, sedimentary structures, and erosion patterns enable reconstruction of the dominant flow direction. The “alluvial formation of Lombrives” and “conglomerates of the gallery of the Counts of Foix” (upper floor) correspond to flow from the Vicdessos towards the Ariège (west to east), in agreement with the slight eastward slope of the Niaux-Lombrives system (Sorriaux, 1982).

Figure 3

Sorriaux (1982) postulated that during the Last Glacial Maximum (Delmas et al., 2012), when coalescent glaciers covered the massifs almost entirely, water flowed through the hypogean karst system from east to west, i.e., from Ariège to Vicdessos. During the following Garrabet deglaciation stage, waters abandoned the upper levels of the karst due to glacial retreat and associated glacial disjunctions. Melt waters of the Ariège and Vicdessos then joined the Lombrives lower level and flowed to Sabart. During the final stages of the Garrabet cycle, the surface of the Ariège glacier only reached an altitude of 600 m a.s.l., and the Vicdessos glacier was confined to its high valley. Therefore, at that time, waters could only penetrate the system at the level of the Lombrives cave inlet.

Subsequent to the alluvial deposits, these galleries also contain red clay formations that testify to the occurrence of lakes. This necessitates that the previously described glacial levels do not strictly correspond to the stepped galleries.

Dating of the alluvial sediments deposited in this karst system therefore better constrains its functionality and geomorphological evolution.

3.2- Sédour, Calamès, and Quié de Lujat massifs

The Sédour and Calamès massifs (Figs. 4 and 5, respectively) were originally constituents of the same limestone units, but have since been intersected and progressively entrenched by the Saurat River. This implies that data obtained in the few preserved cavities (due to receding walls) can be correlated. Alluvial deposits in these massifs are highly altered and rubified, with crystalline pebbles.

Inventoried cavities of the Sédour massif (Fig. 4) indicate their consistent staging, though less-accessible cavities do not contain intrakarstic sediments. The most developed cavity is the Bédeilhac cave, which contains rupestrial art and is the only cave in the investigated massifs with galleries wide and high enough to have served as an aircraft hangar during World War II. Hangar installation at the entrance of the cavity exposed a large section of alluvial deposits, which range from fairly rubified medium sands to altered crystalline pebbles. Clay deposits are also numerous, possibly indicating phases of transient damming. Chrono-stratigraphic correlation of these deposits is difficult; although correlating this and the Niaux-Lombrives levels seems reasonable, although the presence of faults and the proximity of a formerly exploited Triassic gypsum formation render this correlation speculative. However, numerous circulations in the epiphreatic regime (lapiés, circular pools, vault channels, and scallops) provide opportunities for improving the correlation relationships.

Figure 4

The Bouicheta cave opens on the western flank of the Sédour massif and developed mainly along a NE-SW axis over a length of approximately 85 m. Because this cavity has undergone several excavations and has served as a sheep fold, the organization of the sedimentary deposits has been disturbed. Nevertheless, old stalagmitic floors surmount silty deposits, and an important concretion episode is preserved.

The Moutons cave developed along the same axis as the Bouicheta cave, but over a length of approximately 20 m. Inside a low room nearly as long as it is wide, large portions of

stalagmitic floors are present. The walls of this room present deep, circular pool shapes indicating an ancient epiphreatic regime, and a conduit leads to alluvial deposits.

Cavities in the Calamès massif (Fig. 5) are relatively short. The Quarry cave, at the base of the limestone cliff along Saurat River, developed over a length of ~5 m, although the wall has retreated by ~30 m due to anthropic exploitation. The remaining vault section is fairly wide. It seems to be a drain that formed in an epiphreatic regime. The observed lapiés may have formed on the banks of an aggraded river, and fills are alluvial deposits (highly altered pebbles surmounted by graded sandy levels) that contain intercalated relics of stalagmitic floors. A lacustrine and deltaic level that originated in the Bédeilhac palaeolake faces the cavity. These deposits comprise varves with silty strata, some sandy and gravelly occurrences, and pebbled levels. Two morainic blocks are located at the top of the sequence.

Figure 5

Cavities on the south side of the massif are slightly more developed. The length of the Enchantées cave is approximately 45 m, and its shape displays numerous indices of epiphreatic regime with corrosion at the vaults. Its abundant fillings comprise rubified sandstone claddings on the walls and vaults, and smaller clasts are altered. Two erratic blocks lie at the porch entrance.

Further upstream, the limestone cliff opens onto several small porches. Here, three small, short caves (~50 m in length) are presently well separated. However, due to their shared NW-SE orientations and the similarity of the observed morphologies, this gallery was probably intersected by the recession of the wall of the Esplourgues cave. Similar to the Enchantées cave, flowstone formation has been intense and stalagmitic floors are inserted in varied fillings ranging from laminated strands to powdery pebbles clad to the walls. The morphologies of the walls and vaults are characteristic of epiphreatic flows. However, at the most perched entrance, fluid escape structures are observed as coarse to highly altered and rubified pebbly deposits.

The Quié de Lujat massif is poorly karstified compared to the other massifs in the study area, and few relics of horizontal conduits remain. Typical morphologies of epiphreatic circulations, including scallops and deep circular pools, are visible at the entrance to the cavity, indicating a possible resurgence. Variously cemented coarse alluvial deposits remain, including highly altered and rubified crystalline pebbles. This cavity, perched at 1,100 m a.s.l., was below the maximum level of the Ariège glacier during the Foix glacial cycle (Sorriaux et al., 2016).

Splouga de Souloumbrié, in the eastern slope of Quié de Lujat massif, is a cavity that also presents many typical flow morphologies (scallops and circular pools). The main gallery is obstructed by a rockfall, which may truncate the small network.

4- Materials, methods, and sampling strategy

4.1- Description of the studied caves

Many caves in the studied area (Fig. 6; Table 1) are hidden and difficult to access due to vegetation cover. These caves are also subject to heightened protection measures due to their archaeological interest or their importance to the preservation of specific troglobite species. Thus, only three cavities in Calamès massif, three in Sédour massif, two in Quié de Lujat massif, and two in Cap de la Lesse massif could be sampled.

4.1.1- Epiphreatic model and chronology of valley deepening

The epiphreatic model of Audra and Palmer (2011, 2013), on which our work is based, considers three different zones: the vadose zone, the epiphreatic zone (in which the water table fluctuates), and the phreatic zone. This model assumes that recharge occurs via sinking streams, dolines, and the epikarst, a branching cave system established in the vadose zone above the water table. Vadose passages include shafts and canyons. Groundwater flows along a relatively gentle gradient to springs at the water table level in nearby valleys. Most phreatic passages are tubular and form at or slightly below the water table, although many exhibit vertical loops. During floods, phreatic passages may be unable to transmit all the incoming water, causing the development of complex looping overflow routes in the epiphreatic zone. Large phreatic passages develop when the erosional base level remains at a given elevation for an extended period of time (Audra, 1994) and when erosional benches developed. When the base level drops and the surface river erodes downward, phreatic passages tend to drain through diversion routes, and the former phreatic passages indicate the former base level.

Figure 6

The use of karstic systems as markers of palaeo-base levels relies on the localization of certain key morphological factors (Fig. 6B, D), such as characteristic morphologies formed under phreatic or epiphreatic conditions. Cavities of the Tarascon valley mostly contain intrakarstic sediments emplaced by river circulation (see Fig. 6 and Section 3). Allogenic sediments trapped in the karst systems reflect the geomorphological evolution of both the

surface and underground. However, deposits are better preserved underground, especially when concretions, stalagmitic floors, or landslides seal previous deposits.

Figure 7

In most cases, the alluvial sediments we encountered in the cavities were collected and analysed. Reconstituting the stratigraphy is often complex, as only a few residues remain in the visited galleries, except for the larger caves such as Bédeilhac (Fig. 7), Lombrives, and Niaux (Figs. 8, 9). Therefore, we only sampled alluvium cemented against walls that were clearly related to characteristic flow morphologies. In the larger networks of Bédeilhac, Niaux, and Lombrives, more substantial and continuous deposits were sampled.

Figure 8

Figure 9

4.1.2- Attempts to date multiple fillings

In the Niaux-Lombrives-Sabart cave system, fillings are predominantly preserved as discontinuous deposits on the walls of the galleries and in their anfractuosities or connected to the ceiling (Fig. 8). Discontinuities between deposits, limited accessibility, and darkness due to large volumes complicate research on the stratigraphy of these fillings. Because the deposits are occasionally juxtaposed, several generations of alluvial fillings in the Niaux and Lombrives caves are recognizable. Alluvial deposits also show characteristic flow morphologies. Based on the relative chronology and sizes of the observed deposits, large water flows may have filled the galleries without completely removing in-place sediments. These flows were powerful enough to transport blocks (Sorriaux, 1982). Various generations of sediments were collected in areas where stratigraphic and geometric relationships were obvious, the objective being to improve the absolute and relative chronologies of the multiple filling episodes. Samples were also collected in areas previously sampled for petrological studies (Sorriaux, 1982) to obtain additional information via particle size distributions and thin-section observations.

4.2- Burial dating with cosmogenic nuclides

4.2.1. Systematics

Rocks or soils exposed to cosmic radiation at the Earth's surface accumulate terrestrial cosmogenic nuclides (TCNs, such as ^{26}Al, ^{10}Be, or ^{21}Ne) in quartz during their exposure. TCN concentrations in such materials can be calculated as (Braucher et al., 2011):

$$C(t,\varepsilon) = \frac{P_n \cdot \left(1-\exp\left(-t\left(\frac{\rho\varepsilon}{L_n}+\lambda\right)\right)\right)}{\frac{\rho\varepsilon}{L_n}+\lambda} + \frac{P_{\mu s} \cdot \left(1-\exp\left(-t\left(\frac{\rho\varepsilon}{L_{\mu s}}+\lambda\right)\right)\right)}{\frac{\rho\varepsilon}{L_{\mu s}}+\lambda} + \frac{P_{\mu f} \cdot \left(1-\exp\left(-t\left(\frac{\rho\varepsilon}{L_{\mu f}}+\lambda\right)\right)\right)}{\frac{\rho\varepsilon}{L_{\mu f}}+\lambda}, \quad (1)$$

where $C(t, \varepsilon)$ is nuclide concentration (at g^{-1}), t exposure time (yr), ε denudation rate (cm yr^{-1}), and ρ the rock/soil density (g cm^{-3}). P_n, $P_{\mu s}$, and $P_{\mu f}$ are the production rates and L_n (160 g cm^{-2}), $L_{\mu s}$ (1,500 g cm^{-2}), and $L_{\mu f}$ (4,320 g cm^{-2}) (Braucher et al., 2011) the attenuation lengths of neutrons and slow and fast muons, respectively, and λ is the radioactive decay constant (yr^{-1}) of the considered TCN.

The burial dating method is based on the analysis of materials that were initially exposed to cosmic rays before being buried to >10 m depth, where *in-situ* muonic production is reduced to 1% of the total surface production (Braucher et al., 2011). This burial halts the *in-situ* production of TCNs, and their concentrations then evolve by radioactive decay (^{10}Be, ^{26}Al) or remain constant (^{21}Ne). Thus, measuring the concentrations of two cosmogenic nuclides with contrasting half-lives (e.g., ^{26}Al-^{10}Be or ^{10}Be-^{21}Ne) permits computation of the burial duration. The ^{26}Al/^{10}Be ratio can be used to date burial events that occurred during the last ~5 Myr (e.g., Granger & Muzikar, 2001), and ^{10}Be/^{21}Ne to investigate those within the last 15 Myr (e.g., Sartégou et al., 2018).

Burial dating requires that the pre-burial cosmogenic nuclide ratios are known (Blard et al., 2019a; b) and that the surface exposure of quartz, in which TCNs are measured, was long enough to accumulate measurable cosmogenic radionuclide concentrations. In a denudation regime, sediment transport time must have been negligible compared to the exposure duration on a surface prior to burial, and the sediment storage duration within a catchment must have been limited. Finally, burial must have been rapid and deep enough to avoid post-burial production of cosmogenic nuclides. Consequently, this method is well-suited to dating the filling of caves by detrital sediments (e.g., Häuselmann and Granger, 2005; Häuselmann et al., 2015; Sartégou et al., 2018; Häuselmann et al., 2020). Caves provide a near-ideal configuration for such burial duration determinations because post-burial exposure to cosmic rays is negligible in most cases. Furthermore, the galleries of the caves studied herein are always overlain by more than 50 m of rocky material, rendering post-burial production negligible.

In denudation regimes, pre-burial TCN concentrations of river sands are considered to have reached steady state (Lal, 1991), and represent the average of all quartz-bearing rocks outcropping upstream in the drainage basin (Brown et al., 1995). Using the approach of Blard et al. (2006), pre-burial average denudation rates can be determined for an entire drainage

basin by relating the average erosion rate $\bar{\varepsilon}$ to the palaeo-concentration $\bar{C}$ at the moment of burial as:

$$\bar{\varepsilon} = \sum_{i,x} \frac{\bar{P}_i \; L_i}{\rho \; \bar{C}}, \quad (2)$$

where x is the location in the catchment, i refers to the different TCN production pathways (see Eq. (1)), L_i are attenuation lengths for each particle, and $\bar{P}_i$ are the mean basin-wide cosmogenic nuclide production rates, computed from the arithmetic mean of spallogenic and muogenic production using specific scalings for each production pathway as a function of elevation and latitude. Here, pre-burial denudation rates were computed using ^{10}Be concentrations (after correcting for radioactive decay) by using the following production rates: P_n = 4.11 ± 0.19 atoms g^{-1} yr^{-1}, $P_{\mu s}$ = 0.011 ± 0.001 atoms g^{-1} yr^{-1}, and $P_{\mu f}$ = 0.039 ± 0.004 atoms g^{-1} yr^{-1} (Braucher et al., 2011; Martin et al., 2017). We corrected for mass shielding by using the equation of Dunai (2010). Muon contributions based on Braucher et al. (2011) were scaled for altitude only. We calculated production rates for each cell of a 30-m ASTER digital elevation model using a Matlab script and the CREp tool (Martin et al., 2017) and a rock density of 2.5 g cm^{-3}. Areas without surficial quartz-bearing rocks or not linked to the stream network were excluded from the calculations. No correction was performed for ice cover because it only represents a very small proportion of our study area.

Some studies have incorrectly used pre-burial cosmogenic nuclide ratios equal to the production rate ratio when computing burial ages from paired cosmogenic nuclides. In the case of slowly eroded material (<<1 mm yr^{-1}), the pre-burial ratio may be lower than the production ratio, and such a simplification can result in overestimated burial ages. To avoid any bias, accurate burial age calculations should consider the elevation of the quartz-rich watershed and solve the following equation (Blard et al., 2019a, b):

$$\frac{P_1}{N_1} e^{-\lambda_1 \cdot t_{\text{burial}}} - \frac{P_2}{N_2} e^{-\lambda_2 \cdot t_{\text{burial}}} = \frac{\lambda_1 - \lambda_2}{f}, \quad (3)$$

where f is a spatial scaling factor representative of the latitude and altitude of the watershed, t_{burial} is the burial duration (yr), and P_1 and P_2 are the production rates (at g^{-1} yr^{-1}), N_1 and N_2 the concentrations (at g^{-1}), and λ_1 and λ_2 the radioactive decay constants (yr^{-1}) of two cosmogenic nuclides '1' and '2', respectively.

In this study, we employed the following production rates (subscripts indicate the mass number of the nuclide): for P_{10}, we used the most up-to-date global averaged value of 4.11 ± 0.19 at g a^{-1} available in the CREp calculator (Martin et al., 2017); for P_{21}, we used

17.0 ± 0.9 at g a^{-1} deduced from the $^{21}Ne/^{10}Be$ production ratio of 4.12 ± 0.17 (Kober et al., 2007); and for P_{26}, we used 27.3 ± 0.2 at g a^{-1} deduced from the $^{26}Al/^{10}Be$ production ratio of 6.61 ± 0.52 (Nishiizumi et al., 2007; Braucher et al., 2011). The half-lives of ^{10}Be and ^{26}Al are 1.387 ± 0.120 and 0.717 ± 0.017 Myr, respectively (Chmeleff et al., 2010; Korchinek et al., 2010; Granger, 2006; Samworth et al., 1972). The spatial scaling factor f was computed following Stone (2000). Since Equation (3) cannot be analytically solved, we numerically computed t_{burial} using a Monte Carlo approach (10^4 draws), considering that the cosmogenic nuclide concentrations have normal distributions (N_{26}, σ_{26}) and (N_{10}, σ_{10}), where σ_{26} and σ_{10} are their analytical uncertainties. The mean and standard deviation of the 10^4 solutions obtained for t_{burial} were computed to obtain the best solutions and their respective uncertainties (see Table 3 for ^{26}Al-^{10}Be durations). In the case of the ^{10}Be-^{21}Ne pair, Equation (3) can be solved analytically (Blard et al., 2019a, b), and the burial age was then computed as:

$$t_{\text{burial}} = \frac{-1}{\lambda_{10}} \cdot ln\left[\frac{N_{10}}{P_{10}} \cdot \left(\frac{P_{21}}{N_{21}} + \frac{\lambda_{10}}{f}\right)\right]. \quad (4)$$

For both the ^{26}Al-^{10}Be and ^{10}Be-^{21}Ne pairs, burial ages were computed using the present-day watershed elevation of 1,990 m a.s.l. Hypothetical palaeo-elevations of 0 and 4,000 m a.s.l. were also tested to evaluate the impact of elevation changes on the burial ages, which induced a maximum variation of 10% in the computed burial ages. As an acceptable uncertainty, reported burial ages were computed using the modern catchment elevation. Temporal variations in the geomagnetic field integrated over the investigated time periods are assumed to be negligible compared with the total uncertainty in the data.

4.2.2. Measurement of in-situ cosmogenic ^{26}Al and ^{10}Be

All ^{26}Al and ^{10}Be measurements were performed at CEREGE (Aix-en-Provence, France). ^{10}Be and ^{26}Al were extracted from the rock samples following the chemical procedure of Brown et al. (1991) and Merchel and Herpers (1999). Pebbles were crushed and sieved, and the 250-1,000 µm fraction was processed. Quartz was concentrated by magnetic separation and selective dissolution in a 1:2 HCl-H_2SiF_6 mixture. Quartz was decontaminated for atmospheric ^{10}Be by dissolving 30% by mass via three successive HF leaching processes. Pure quartz was spiked with 100 µL of an in-house ^{9}Be carrier (3,025 ± 9 ppm; Merchel et al., 2008) and an adapted amount of a commercial 985-µg/g ^{27}Al carrier. The natural ^{27}Al

concentrations in the dissolved samples were measured by inductively coupled plasma optical emission spectrometry (ICP-OES) on a Thermo Scientific ICAP6500. These analyses were performed using replicate aliquots, two emission lines (394 and 396 nm, axial sight), and two standards (Merck, 999 ± 2 mg/L, and Fluka TraceCert, 985 ± 2 µg/g). Dissolution was completed in concentrated HF.

Due to its high ^{27}Al content, the abundance of muscovite in rocks of the watershed forced us to regularly check the sample purification with a binocular microscope (see Section 4.2.3). If not removed from the quartz before total dissolution, muscovite causes the formation of thick solid crusts from which it is difficult to recover the dissolved aluminium.

BeO and Al_2O_3 were then purified and extracted using a succession of alkaline precipitations and separations on ionic-exchange resins (DOWEX 1X8 100–200 mesh, DOWEX 50WX8 100–200 mesh). Full oxidization was performed at 700 °C for one hour. The obtained BeO and Al_2O_3 oxides were mixed with Nb and Ag conductive powders, respectively, then introduced in a copper cathode to be pressed. The $^{10}Be/^{9}Be$ and $^{26}Al/^{27}Al$ ratios were measured at the French national accelerator mass spectrometry (AMS) facility ASTER. Measured $^{10}Be/^{9}Be$ ratios were calibrated against the NIST standard SRM 4325 ($^{10}Be/^{9}Be = (2.79 \pm 0.03) \times 10^{-11}$; Nishiizumi et al., 2007), and measured $^{26}Al/^{27}Al$ ratios were calibrated against the ASTER in-house standard SM-Al-11 ($^{26}Al/^{27}Al = (7.401 \pm 0.064) \times 10^{-12}$; Merchel and Bremser, 2004). The half-lives used and the standardisation method employed at ASTER (SM-Al-11/07KNSTD) imply that the $^{26}Al/^{10}Be$ spallation production ratio is ~6.61 ± 0.52. Reported analytical uncertainties include counting statistics, machine stability (~0.5% for ^{10}Be; Arnold et al., 2010), and blank correction.

4.2.3. Influence of muscovite on the accuracy of cosmogenic ^{26}Al concentrations

Although our procedure to separate and purify quartz from the sampled sediments was efficient in most cases, it was sometimes insufficient for muscovite-rich samples (reported in italics in Table 3). To quantify the potential impact of the presence of muscovite in supposedly pure quartz mineral samples, we performed tests using samples LO4, LO4b, and LO4c from Lombrives cave (Table 2). LO4 is a quartzite pebble from a sedimentary sequence that was recovered during the carbonate dissolution step of the quartz mineral separation procedure. LO4b and LO4c are derived from the sandy matrix of the same sedimentary sequence, which was particularly rich in quartz. During the various separation steps, muscovites were recovered from this sandy matrix. After elimination of all other accessory minerals, half of the obtained pure quartz mineral sample was processed for reliable ^{26}Al

measurements (LO4b), whereas 141 mg of the recovered muscovites was added to the other half before ^{26}Al analysis (LO4c).

The ^{27}Al concentration of the muscovite-loaded sample (LO4c) is 17 times higher than that of the muscovite-free sample (LO4b; Table 2). Consequently, after accounting for the ^{27}Al spike (9,372.07 ± 46.86 ppm) added to LO4b to obtain a sufficient amount of material for a reliable AMS analysis, the measured $^{26}A1/^{27}A1$ ratios differ by an order of magnitude. Although the amount of added muscovite is negligible compared to ~20 g of dissolved quartz, it significantly distorted the natural ^{27}Al concentration and the measured $^{26}Al/^{27}Al$ ratio. This distortion results in an erroneous ^{26}Al concentration, and thus $^{26}Al/^{10}Be$ ratio and derived burial duration. Eliminating these alumina-rich minerals is therefore paramount. A very thorough separation of mineral phases is necessary for muscovite-rich samples, including high intensity magnetic separation before and after HF-leaching (there is too much static electricity after the HCl-H_2SiF_6 step), flotation, and hand-picking to remove the last leaflets. Another sieving step after the last HF-leaching may be useful because most remaining muscovites are smaller than 250 μm.

Table 2

Samples reported in italics in Table 3 probably have overestimated aluminium concentrations, and thus underestimated burial durations. These results are therefore unreliable and are excluded from further discussion.

4.2.4. Measurement of in-situ cosmogenic ^{21}Ne

Neon isotopic concentrations in quartz were measured at the CRPG (Nancy, France) noble gas laboratory. The same quartz fractions (200–1,000 μm) used for ^{26}Al and ^{10}Be analyses were used for neon analysis. All samples were wrapped in tin foil (melting point, 230 °C) and loaded in the carrousel of the new full-metal induction furnace designed at the CRPG (Zimmermann et al., 2018). The furnace and the entire purification line were then baked at approximately 150 °C overnight under high vacuum. Subsequently, the furnace crucible was degassed at >1500 °C to reduce the neon blanks. Following conclusive validation tests, neon was extracted in a single heating step at ~1400 °C for 20 minutes. The purification line consists of three charcoal fingers cooled with liquid nitrogen (77 K) to trap Ar, Kr, Xe, and chemically active gases including N_2, O_2, and CO_2 (Zimmermann et al., 2015). Three Ti-sponge getters also permit trapping of the remaining reactive gases (particularly N_2, O_2, CO_2,

493 and H_2). Ne was then cryofocused at 30 K before being released at 100 K and input into the
494 mass spectrometer for analysis.

495 The purified gas was input into the analyser, and ^{22}Ne, ^{21}Ne and ^{20}Ne concentrations
496 were measured using high-sensitivity mass spectrometers: the Helix-MC+^{TM} (two aliquots of
497 sample SO1) and the Helix-SFT^{TM} (all other samples). Neon isotopic concentrations were
498 measured by simultaneous multi-collection on the Helix-MC+^{TM} and by peak jumping mass
499 spectrometry with the electron multiplier of the Helix-SFT^{TM}.

500 During mass spectrometry analyses, a getter trap minimized the contribution of CO_2^{++}
501 on the ^{22}Ne signal and maintained a low H_2 abundance, which can produce an isobaric
502 interference of $^{20}NeH^+$ on ^{21}Ne (Honda et al., 2015). A charcoal finger is also present in the
503 mass spectrometer to trap CO_2, H_2O, and Ar (77 K). The sensitivity of the mass spectrometer
504 was determined using an in-house gas standard of atmospheric composition. After each
505 analysis, any remaining gas was pumped. Neon isotopic concentrations were corrected for hot
506 furnace blanks and instrumental mass fractionations. Isobaric interference of $H_2{}^{18}O$ on ^{20}Ne
507 was determined for each sample by measuring $H_2{}^{16}O$ and assuming a $H_2{}^{16}O/H_2{}^{18}O$ ratio of
508 495 (Honda et al., 2015); this ratio corresponds to a correction smaller than 0.1%.

509 The neon extracted from the quartz samples is generally produced from a mixture of
510 cosmogenic neon and atmospheric neon. Cosmogenic neon is mainly located in the lattice,
511 while atmospheric neon is mainly trapped in fluid inclusions and/or adsorbed on grain
512 surfaces. The position of a given sample in the three-isotope plot indicates whether it belongs
513 to the spallation-air mixing line (Fig. 10). In practice, we determined the cosmogenic
514 concentrations $^{21}Ne_{cos}$ as (Vermeesch et al., 2015):
515

516 $$^{21}\mathrm{Ne}_{\mathrm{cos}} = R_{\mathrm{c}} \times {}^{20}\mathrm{Ne}_{\mathrm{m}} \times \frac{R_{\mathrm{m}} - R_{\mathrm{a}}}{R_{\mathrm{c}} - R_{\mathrm{a}}}, \quad (5)$$

517 where $^{20}Ne_m$ (at g^{-1}) is the measured amount of ^{20}Ne, R_c = 0.8 is the cosmogenic $^{21}Ne/^{20}Ne$
518 production ratio, R_m is the measured $^{21}Ne/^{20}Ne$ ratio, and R_a = 0.002905 is the atmospheric
519 $^{21}Ne/^{20}Ne$ ratio (Honda et al., 2015).

520 Aliquots of the quartz standard CRONUS-A measured during the same session yielded
521 a mean ^{21}Ne excess of (3.38 ± 0.05) × 10^8 at g^{-1}, in agreement with the reference
522 concentration of (3.48 ± 0.10) ×10^8 at g^{-1} (Vermeesch et al., 2015).
523

524 **5- Results**

525

5.1- Cosmogenic ^{26}Al, ^{10}Be results, ^{26}Al/^{10}Be burial durations and palaeodenudation rates

All ^{26}Al and ^{10}Be results are presented in Table 3. Most samples yielded ^{10}Be/^{9}Be ratios significantly above the blank value (blanks ranged from 1.5×10^{-15} to 3.0×10^{-15}). These ratios indicate ^{10}Be concentrations ranging from $(8 \pm 1) \times 10^3$ to $(114 \pm 18) \times 10^3$ at g^{-1}. Uncertainties on ^{10}Be concentrations range from 6 to 41%. Some samples had ^{27}Al/^{26}Al ratios below the analytical detection limit (~2×10^{-15}; blank value, 2.2×10^{-15}), suggesting burial durations longer than 6.5 Myr. These samples, for which only ^{10}Be concentrations were measurable, are from the highest caves (Bouicheta, Moutons, Mirouge, and Souloumbrié). Otherwise, ^{26}Al concentrations varied between $(3 \pm 3) \times 10^3$ and $(34.8 \pm 4.1) \times 10^4$ at g^{-1}. Uncertainties on ^{26}Al concentrations ranged from 12 to 100%.

^{26}Al/^{10}Be burial durations ranged from 0.7 ± 0.4 to 8.8 ± 1.7 Myr. The durations determined for Lombrives and Niaux caves are scattered, which is not surprising given the evidence of several phases of filling. However, the burial durations calculated for Ni13-08, Ni13-10, Ni13-15, Ni13-20, and Ni13-23 in Niaux cave are not internally consistent and do not agree with the U-Th ages obtained by Sorriaux (1981, 1982, in press) and Bakalowicz et al. (1984) for most of the stalagmitic floors that embed these alluvial formations. Indeed, although they belong to the same depositional sequence that can be followed continuously over a few meters, the burial durations calculated for Ni13-23 and Ni13-20 are significantly different. Therefore, alluvial deposition phases in Niaux cave cannot generally be discriminated. In rare cases, calculated burial durations are not consistent with the relative chronology, particularly the latest deposited sequences LO1 and Ni12-02, for which the burial durations are different. The most problematic finding, however, is that equivalent deposits in the Niaux-Lombrives-Sabart cave system return different burial durations depending on the cave considered. These inconsistencies are not observed in the Bédeilhac cave, which may be part of a single level and therefore evolved under similar conditions. However, no U-Th dating is available for this cavity, and fewer cosmogenic burial dates were obtained than in Niaux cave. Furthermore, the stratigraphy in the Bédeilhac cave is quite ambiguous. Therefore, firmly attributing the observed variations to a sampling bias is difficult.

Table 3

Initial concentrations obtained for samples from caves of the Calamès massif produced coherent ages at approximately 3–4 Ma. However, the analysed samples (CALA 14-02, 14-04, 14-05) contained abundant muscovite. Subsequent measurements of muscovite-free samples taken at the same sites (CALA 14-01 and 14-03) indicate significantly longer burial

durations consistent with those of samples from Bédeilhac cave. Therefore, eliminating muscovite is crucial before performing any cosmogenic ^{26}Al measurements.

Palaeodenudation rates derived from the measured ^{10}Be and ^{26}Al concentrations range from 3 ± 1 to 797 ± 101 mm/kyr (Table 3).

5.2- Cosmogenic ^{21}Ne results, ^{10}Be/^{21}Ne burial durations and palaeodenudation rates

Neon isotopic concentrations and ratios, and cosmogenic ^{21}Ne concentrations are reported in Table 4, and ^{10}Be/^{21}Ne burial durations and palaeodenudation rates in Table 5.

Table 4

Cosmogenic ^{21}Ne concentrations computed with Equation (5) range from (1.20 ± 0.19) × 10^7 at g^{-1} to (2.20 ± 0.26) × 10^7 at g^{-1}. Relative uncertainties range from 12 to 48% and mainly result from the atmospheric ^{21}Ne correction. These $^{21}Ne_{cos}$ concentrations imply present ^{21}Ne/^{10}Be ratios significantly larger than the surficial ^{21}Ne/^{10}Be production ratio of 4.12 ± 0.17 (Kober et al., 2007). These results indicate significant burial durations that range from 6.8 ± 0.3 to 12.6 ± 0.3 Myr (Table 5). Paleodenudation rates computed from the radioactive decay-corrected ^{10}Be concentrations range from 2.8 ± 0.3 to 4.8 ± 0.6 mm kyr^{-1}.

Table 5

The measured neon isotopic ratios are, within uncertainties, compatible with the spallation-air mixing line in the neon three-isotope diagram, suggesting that atmospheric and spallogenic neon are probably the main components (Fig. 10). However, the uncertainty of the measured ^{22}Ne/^{20}Ne ratio is too high to ensure the absence of nucleogenic ^{21}Ne. Hence, the excess ^{21}Ne concentrations computed with Equation (5) assuming binary mixing must be considered as maximum cosmogenic ^{21}Ne concentrations. The potential accumulation of nucleogenic ^{21}Ne from the $^{18}O(\alpha,n)^{21}Ne$ reaction in quartz can also be considered and computed. The production rate of this reaction is proportional to the U and Th concentrations in the quartz samples (Niedermann, 2002). Observations suggest that U and Th concentrations are higher in secondary quartz coatings or diagenetic silica cements than in crystalline quartz (Balco et al., 2019). Hence, to compute an upper boundary for this nucleogenic contribution, we consider the higher values of reported U and Th concentrations in unetched quartz, i.e., 0.40 ± 0.14 ppm U and 1.06 ± 0.49 ppm Th (Balco et al., 2019, and references therein), which

yield a nucleogenic ^{21}Ne production rate of (0.10 ± 0.03) × 10^6 at g^{-1} yr^{-1} (Balco et al., 2019). The closure temperature of the analysed quartz (~0.5 mm diameter) is ~100 °C (Shuster and Farley, 2005), assuming a cooling rate of 10 °C/Myr. U-Th/^{4}He thermochronometry (Milesi et al., 2020; Maurel et al., 2008) established the exhumation history of the granitic and metasediment massif drained by the Ariège river. They established that this material cooled below the 100 °C isotherm at 40 ± 20 Ma. Combined with the production rate of (0.10 ± 0.03) × 10^6 at g^{-1} yr^{-1}, this yields a maximum nucleogenic ^{21}Ne build-up of (4.2 ± 2.5) × 10^6 at g^{-1}. This maximum nucleogenic ^{21}Ne contribution represents between 19 and 34% of the ^{21}Ne excess computed with Equation (5). Given the non-linearity between the burial age and the ^{10}Be/^{21}Ne ratio (Eq. (4)), this correction should only lower the ^{10}Be/^{21}Ne burial durations by 13 to 19% (Table 5). Because these corrected ages accounting for the maximum theoretical nucleogenic ^{21}Ne contribution are compatible with the non-corrected ages at the 2-sigma level, we chose to consider ^{10}Be/^{21}Ne burial durations not corrected for this nucleogenic ^{21}Ne build-up in the following discussion.

Figure 10

6- Discussion

6.1- Dispersion among ^{26}Al/^{10}Be and ^{10}Be/^{21}Ne burial durations in caves: implications for cave filling dynamics and the accuracy of this dating method

^{26}Al/^{10}Be and ^{10}Be/^{21}Ne burial durations observed in the same caves are characterized by intersample dispersions that are larger than the analytical uncertainties. In particular, ^{26}Al/^{10}Be data from the Niaux-Lombrives-Sabart karstic system (114–142 m above Ariège River) are characterized by an important age dispersion that ranges from <0.5 to >8 Ma. Three causes may explain the large dispersion of this dataset.

First, incomplete muscovite removal may have biased ^{26}Al measurements and thus the accuracy of the computed ^{26}Al/^{10}Be burial durations. Although we took special care during muscovite removal, we cannot rule out this analytical bias that results in under- and overestimated ^{26}Al concentrations and ^{26}Al/^{10}Be burial durations, respectively.

Second, the diachronous filling of these caves spanned several million years (e.g., Häuselmann, 2007; Sartégou, 2017; Sartégou et al., 2018), consistent with thin-section observations of several coexisting angular and more rounded quartz populations in various states of deterioration according to the deposit (Sorriaux, 1982). The more weathered quartz population, *a priori* of glacial origin, were reworked during alluvial transport phases. These quartz present fractured faces and grinding traces. The presence of materials of different origins in the same stratigraphic layers suggests that high-energy flooding phases within the cavity mixed fresh and older sediments (e.g., Häuselmann, 2007). The high energy of these flows is attested by the presence of blocks (> 1 m^3). The dispersion of $^{26}Al/^{10}Be$ burial durations in a single cave is consistent with Sorriaux's (1982) results and suggests that the studied karstic networks recorded several alluvial phases during the last glacial stages. These processes are probably attributed to climatic variability, particularly the influence of Quaternary glacial cycles on denudation and sediment transport dynamics. As proposed by Sorriaux (1982), the glacial origin of these formations and processes indicates a base level rise during the glaciation phases, as observed in the Austrian Northern Calcareous Alps (Plan et al., 2009). In addition, exchanges between network levels likely occurred. Indeed, because a shaft links the two levels of Lombrives cave, material from the upper level that contributed to the formation of this shaft "contaminated" the lower level. The review by Audra et al. (2006) presents a useful discussion on the dynamics of karst filling.

Third, since the analysed detrital material is probably a mixture of heterogeneous sediments derived from various sources, it may have been affected by contrasted and successive burial-exposure cycles within the watershed before entering the caves. Sediments subjected to multiple exposure-burial cycles before their definitive burial in a cave have $^{26}Al/^{10}Be$ ratios lower than the theoretical ratio used to compute the ages of the studied deposit (e.g., Laureano et al., 2016; Sartégou et al., 2018). This implies that a significant proportion of our computed burial durations may be overestimated. Indeed, some of the $^{26}Al/^{10}Be$ burial durations derived from detrital samples are older than the U-Th ages of the carbonate stalagmitic floors that bracket these deposits (Fig. 11).

The bias toward older ages is, in theory, larger for the ^{10}Be-^{21}Ne dating system than for the ^{26}Al-^{10}Be pair because the stability of ^{21}Ne implies that the observed concentration of this cosmogenic nuclide integrates all previous exposure-burial cycles. Consistently, our $^{26}Al/^{10}Be$ burial durations are on average younger than $^{10}Be/^{21}Ne$ ages measured in the same caves (Fig. 12, Tables 2 and 4). Hence, the youngest $^{26}Al/^{10}Be$ ages are probably more representative of the last cave filling event for the Niaux-Lombrives-Sabart and Enchantées

caves. Indeed, the $^{26}Al/^{10}Be$ age distributions of these caves have modes respectively centred at approximately 3 and 5 Ma (Fig. 12). However, this cave level is characterized by multiple phases of deposits. Because the burial ages of deposits in the upper Moutons caves (385–576 m above Ariège River) are too old for $^{26}Al/^{10}Be$ dating, we must rely on $^{10}Be/^{21}Ne$ burial durations to date the last filling of these caves, considering that these $^{10}Be/^{21}Ne$ durations are probably maximum age constraints.

Figure 11

Figure 12

Our data and their potential interpretation have strong implications for the significance and accuracy of the determined burial durations. To ensure that the age of karstic alluvium is representative of the incision rate of a valley, different approaches and geochronological methods should be combined whenever possible, including stratigraphy, karstic geomorphology, geochemical and/or luminescence dating (to determine burial duration and provenance), and particle size and microscopic analyses. Notably, complementary absolute ages of carbonate concretions are quite useful. Electron spin resonance dating of samples from the Calamès and Sédour massifs was attempted, but found to be unreliable in this area (see Chapter 6 of Sartégou, 2017, in which the methodological limits are discussed); therefore, we exclude those data from further discussion.

6.2- Relationships between incision process, stepped karstic systems, the water table, and epiphreatic galleries

Our chronostratigraphic interpretation of the studied caves relies on the assumption that large karstic networks formed in a single step at the water table. According to this simple model, once a horizontal network has been formed, the water table drops and the old networks are abandoned and fossilized. New karstic networks are then initiated at the level of the new water table. Each cave level at a given elevation is thus associated with specific geomorphological and climatic conditions that are favourable to its development. However, network formation is likely much more complex in stepped sub-horizontal caves that bear markers of successive circulation episodes in (epi-)phreatic regimes. In such cases, individual

692 cave levels may have different implications for the system development (e.g., Mocochain et
693 al., 2009; Audra and Palmer, 2011, 2013).
694 In the Ariège valley, the Niaux-Sabart-Lombrives network is typical of old karst
695 networks that underwent multiple filling phases over more than 100 kyr under the control of
696 successive glaciation stages. The speleogenesis of these networks probably simply occurred at
697 the level of the water table (records discussed in Section 3.3). However, subsequent major re-
698 flooding events seem to have profoundly reshaped some of the main karstic networks. Thus,
699 the entire geochronological dataset of the Ariège caves was not solely controlled by valley
700 incision since the Miocene. This must be considered when interpreting the significance of
701 some burial durations, such as for samples Ni12-02, Ni13-08, Ni13-10, Ni13-12, Ni13-13,
702 LS1, and LO1. As our interpretations are based on solid petrographic and morphological
703 arguments, we consider them to be sound interpretations based on the present state of
704 knowledge.
705 If these considerations are correct for large kilometric networks, confirming their
706 validity for smaller hectometric cavities (Esplourgues, Enchantées, and Bédeilhac caves) is
707 difficult because sedimentary sections are rarely visible and deposits do not appear
708 polyphased. The relatively low dispersion of the $^{26}Al/^{10}Be$ burial durations in these caves (Fig.
709 12) suggests that the filling of these caves occurred in a single depositional phase.
710 Therefore, we employ a cautious approach to interpreting our data, and consider the
711 size and shape of the gallery before extrapolating the measured burial durations to an entire
712 gallery level. In the following section, we rule out suspect $^{26}Al/^{10}Be$ and $^{10}Be/^{21}Ne$ burial
713 durations by considering gallery morphologies and stratigraphic and petrological constraints.
714
715 **6.3- Ariège River valley incision since 13 Ma (Langhian)**
716 Considering the above-mentioned potential complications, our calculated burial
717 durations indicate the likely evolution of Tarascon valley incision since the Langhian (c. 13
718 Ma), which corresponds to the burial duration derived from a sample taken from Mirouge
719 cave, the most perched sampled cavity (Fig. 12). From the Langhian to the Tortonian, the
720 range of possible incision rates deduced from $^{10}Be/^{21}Ne$ burial durations vary between 80 and
721 310 m Myr^{-1}. These rates were measured in three samples from the Mirouge, Souloumbrié,
722 and Moutons caves (samples LUJ1, SO1, and MOU1). These poorly constrained results may
723 be explained by the low preservation of cavities at these elevations and the small amount of
724 alluvium to be sampled. From the Tortonian to the Mio-Pliocene transition, the range of
725 possible incision rates varies from 20 to 30 m Myr^{-1}. A "continuous" incision rate of

approximately 50 m Myr^{-1} from the Langhian to the Mio-Pliocene transition is quite plausible, and could have established the karst networks if it were moderated by more or less pronounced stationary phases (Audra, 1994). Inducing incision rates after the Mio-Pliocene transition is difficult due to perturbations introduced by glacial re-flooding events. From the Tortonian (~9 Ma) to the present, several scenarios are possible. Considering the upper and lower bounds of the burial durations obtained in the Massif du Calamès, we estimate maximum and minimum Plio-Quaternary incision rates of ~200 and ~25 m Myr^{-1}, respectively.

This range of incision rates is consistent with those estimated in the easternmost Têt River valley (Sartégou et al., 2018), further west in the Salat watershed of the Arbas massif since the Pliocene (110 m Myr^{-1}; Genti, 2015), and on the Garonne terraces (maximum rates of ~46 m Myr^{-1}; Stange et al., 2014). Moreover, our dataset is consistent with reconstructions of palaeo-weathering surfaces and their associated age ranges (e.g., Lagasquié, 1963; Monod et al., 2016a, b). The weathering profiles associated with highly elevated and low-relief surfaces in the study area may have developed between the Eocene-Oligocene and the late Miocene (e.g., Calvet, 1996) and seem to be related to the Pyrenean orogeny. Monod et al. (2016a, b) considered that the Aston-Beille surface was denuded by up to 50 m since the Miocene and partially dissected by incision, and our dataset seems to corroborate these assumptions. By extrapolation of these incision rates, the Beille plateau (1,800–2,000 m high) would have formed between the Rupelian (~32 Ma) and the middle Burdigalian (~18.5 Ma).

Because incision during the Langhian-Serravallian period may be attributed to either an undocumented uplift or a global eustatic base-level fall (as during the Langhian-Serravallian transition; Haq et al., 1987), the mechanisms driving incision at that time remain unknown. Variations in incision rates seem less marked in the Ariège than in the Têt River valley (Sartégou et al., 2018), which may indicate a more "linear" process, despite the numerous possible scenarios. This finding suggests a possible post-orogenic rejuvenation of the relief during the Langhian-Messinian. On the other hand, the variable incision rates observed in the Têt River valley, which was slightly glaciated and is connected to the Mediterranean Sea, imply that the contribution of external forcings cannot be excluded there. Further west along the Pyrenees, notably in the Eaux-Chaudes and Balaïtous-Panticosa massifs, Bosch et al. (2016) used thermochronological data to document significant exhumation between 20 and 30 Ma. They also used apatite (U-Th)/He data to document accelerated exhumation of the Balaïtous-Panticosa granitic massif at ~8–9 Ma. Indeed, previous studies of the southern foreland basin documented post-orogenic cooling (Jolivet et

al., 2007; Labaume et al., 2016; Bernard et al., 2019). Because these areas are all in the central Pyrenees, this last exhumation event seems coincidental with the recorded incision.

Attributing incision during more recent periods (especially during the Tortonian to Pliocene) to a single mechanism remains difficult. Stange et al. (2014), Delmas et al. (2015), and Mouchené et al. (2017) suggested the dominance of external forcings during the Quaternary. Isostatic rebound, which is related either to surface processes such as denudation (Genti et al., 2015) or to the suppression of the thick ice layer present in these internal zones during the last glacial maximum (Crest, 2017), may explain part of the observed uplift.

6.4- Palaeodenudation rates

Figure 13

Our derived palaeodenudation rates for the Ariège River valley characterize a significant increase in denudation between the Langhian (14 Ma) and the Pleistocene (2.6–0 Ma) (Table 3, Fig. 13). Palaeodenudation rates ranged from 3 to 10 mm kyr^{-1} between 13 and 6 Ma, from 10 to 50 mm kyr^{-1} during the Pliocene and Pleistocene, and exceed 100 mm kyr^{-1} (0.1 mm yr^{-1}) during the Holocene. Modern ^{10}Be-derived denudation rates for river sands of rivers draining the Pyrénees and Massif Central are 50–300 and 50–100 mm kyr^{-1}, respectively (Molliex et al., 2016; Olivetti et al., 2016; Sartégou et al., 2018).

Plio-Pleistocene palaeodenudation rates of 3–10 mm kyr^{-1} are similar to those observed in the nearby Têt River valley. However, the Ariège records a greater increase in denudation than the Têt record (Sartégou et al., 2018). These findings suggest that increased denudation was triggered by the global cooling that occurred during this time period due to the appearance of high-amplitude and high-frequency Pleistocene glacial cycles (Molnar, 2004; Herman et al., 2013). However, the extreme increase of denudation rates in the Ariège record (i.e., by nearly three orders of magnitude) is rather peculiar, and suggests that climate was not the only factor influencing denudation in this basin; uplift and enhanced geodynamic flux in a collisional regime are more probable forcings. This interpretation appears consistent with apatite fission track data acquired in the nearby Arize, Trois-Seigneurs, Aston, and Bassiès massifs (Gunnell et al., 2009; Vacherat et al., 2016). Furthermore, (U–Th)/He dating of zircons and apatites show that minimal denudation occurred since the Eocene-Oligocene (Morris et al., 1998; Fitzgerald et al., 1999; Sinclair et al., 2005; Denèle, 2007; Jolivet et al., 2007; Gunnell et al., 2009; Vacherat et al., 2016). The agreement between long-term

exhumation data and our data therefore suggests a predominantly tectonic control on Pyrenean incision. This interpretation is consistent with long-term ^{10}Be-derived palaeodenudation rates in Central Asia, which was uplifted during the Alpine collision (e.g., Puchol et al., 2017).

On a shorter timescale, previous cosmogenic denudation rate estimates in the northern Pyrenees were mainly derived from piedmont alluvial terraces (Stange et al., 2014; Delmas et al., 2015; Nivière et al., 2016; Mouchené et al., 2017) or from preliminary dating of alluvial cave sediments (Genti, 2015; Sartégou et al., 2018). Pleistocene and Holocene alluvial terraces have primarily yielded denudation rates similar to those presented herein (Delmas et al., 2015; Mouchené et al., 2017). Denudation rates determined from Ariège tributary deposits (Aston-Beille catchment) are also consistent with our data (Crest, 2017).

Grain size-dependent ^{10}Be concentrations (e.g., Puchol et al., 2014) were not observed in this work. The most probable cause of significantly higher palaeodenudation rates is therefore the origin of the clasts. Certain similar lithologies are observed at separate and very remote locations in the watershed. In the case of these lithologies, discriminating whether pebbles originate from proximal or distal locations in the catchment and whether they were produced from steeper or gentler slopes, during particular climatic events, or during stochastic events (e.g., landslides, flash floods) is therefore not possible.

7- Conclusions

We proposed a geochronological framework for detrital materials filling caves developed in the Ariège River valley based on the ^{26}Al/^{10}Be and ^{10}Be/^{21}Ne burial chronometers. Although our results display significant scatter, they are coherent with the stratigraphic order and allow us to quantify the incision of the Ariège River valley since the Langhian age. Incision probably began during the early Miocene, at c. 13 Ma, due to geodynamic mechanisms that have not yet been identified. The average incision rate of the Ariège River deduced from our cave dating is on the order of 13–50 m Myr^{-1}, similar to incision rates in the Salat valley to the west (Genti, 2015) and the Têt valley to the east (Sartégou et al., 2018).

Our data highlight a broad dispersion of burial durations within a single karstic network, as illustrated by the Niaux-Lombrives network in the Cap de la Lesse massif. The Niaux-Lombrives-Sabart stepped karstic system is an ancient karst with polyphased fillings spanning several glaciations. During the last glacial cycle, the Ariège River valley was almost completely covered by ice, which, upon melting, generated new floods in previously

developed karstic networks (as observed in the Alps; Audra et al., 2006; Plan et al., 2009). These re-flooding events mixed newly buried sediments with sediments that had been shielded from cosmic radiation for several million years. Our data therefore include notable uncertainties that arise from the complexity of the investigated systems instead of analytical biases. After accounting for these potential complications, our data demonstrate the preponderant influence of external forcings on incision. Our results also illustrate that not all stepped karstic systems are directly representative of the incision processes in nearby valleys.

This work demonstrates that ^{10}Be-^{21}Ne paired nuclides are a useful complement to the ^{26}Al-^{10}Be cosmogenic pair because the burial duration method can be extended beyond 5 Ma, and coherent ages can be obtained to 15 Ma.

Acknowledgements

This work was funded by the BRGM within the framework of the RGF Pyrenees program. We especially thank the Speleological Committee of Ariège (CDS09), and in particular the Spéléo Club of Haut-Sabarthez (SCHS) and the Spéléo Club of the Arize (SCA, Saurat cave), for sharing their invaluable knowledge of the area and their topographic dataset, and Luc Wahl who accompanied us during several sampling campaigns. We thank Max Nicol for his knowledge of Mirouge cave. This work was only possible with the cooperation of DRAC Midi-Pyrénées, which authorized P. Sorriaux to observe and sample Niaux cave within the framework of the "sampling of pre-Würmian deposits for cosmogenic nuclides and U/Th dating" project. Mr. Bodin allowed us to visit and sample Lombrives cave. René Gailli, the curator of the Bédeilhac cave, and Marina Laborde allowed us to walk and sample at our leisure. We sincerely thank Martin Stokes, Jo De Waele, Darryl Granger, Fin Stuart, and Philipp Häuselmann for constructive comments that improved the quality of the manuscript. The ASTER AMS national facility (CEREGE, Aix-en-Provence, France) is supported by the INSU/CNRS, the ANR through the "Projets thématiques d'excellence" program for the "Equipements d'excellence" ASTER-CEREGE action, and IRD.

References

Arnold, M., Merchel, S., Bourles, D.L., Braucher, R., Benedetti, L., Finkel, R.C., Aumaître, G., Gottdang, A., Klein, M., 2010. The French accelerator mass spectrometry facility ASTER: Improved performance and developments. Nuclear Instruments and Methods in Physics Research Section B 268, 1954–1959. https://doi.org/10.1016/j.nimb.2010.02.107

Audra, P., 1994. Karsts alpins : Genèse de grands réseaux souterrains. Karstologia Mémoires 5.

Audra, P., Bini, A., Gabrovsek, F.,Häuselmann, P., Hoblea, F., Jeannin, P.-Y., Kunaver, J., Monbaron, M., Sustersic, F., Tognini, P., Trimmel, H., Wildberger, A., 2006. Cave genesis in the Alps between the Miocene and today: a review. Annales de Géomorphologie / Annals of Geomorphology / Zeitschrift für Geomorphologie, Schweizerbart und Borntraeger 50 (2), 153-176.

Audra P., Palmer A.N., 2011. The pattern of caves: controls of epigenic speleogenesis. Géomorphologie : relief, processus, environnement 4, 359-378. https://doi.org/10.4000/geomorphologie.9571

Audra P., Palmer A.N., 2013. The Vertical Dimension of Karst: Controls of Vertical Cave Pattern. In: John F. Shroder (Editor-in-chief), Frumkin, A. (Volume Editor) Treatise on Geomorphology, Vol 6, Karst Geomorphology, San Diego, Academic Press, 186-206.

Babault, J., van den Driessche, J., Bonnet, S., 2005. Origin of the highly elevated Pyrenean peneplain. Tectonics 24, TC2010. https://doi.org/10.1029/2004TC001697

Bakalowicz, M., Sorriaux, P., and Ford, D.C., 1984. Quaternary glacial events in the Pyrenees from U-series dating of speleothems in the Niaux-Lombrives-Sabart caves, Ariège, France. Norsk geogr. Tidsskr. 38, 193-197. https://doi.org/10.1080/00291958408552125

Balco, G., Blard, P.-H., Shuster, D., Stone, J., Zimmermann, L., 2019. Cosmogenic and nucleogenic ^{21}Ne in quartz in a 28-meter sandstone core from the McMurdo Dry Valleys, Antarctica. Quaternary Geochronology 52, 63-76. https://doi.org/10.1016/j.quageo.2019.02.006

Bernard T., Sinclair H. D., Gailleton B. Mudd, S.M., Ford M., 2019. Lithological control on the post-orogenic topography and erosion history of the Pyrenees. Earth and Planetary Science Letters 518, 53-66. https://doi.org/10.1016/j.epsl.2019.04.034

Blard P.-H., Bourlès D., Lavé J., Pik R., 2006. Applications of ancient cosmic-ray exposures: theory, techniques and limitations. Quaternary Geochronology 1, 59-73.

Blard P.-H., Lupker M., Rousseau M., Tesson, J., 2019a. Two MATLAB programs for computing paleo-elevations and burial ages from paired-cosmogenic nuclide, MethodsX 6, 1547-1556.

Blard P.-H., Lupker, M., Rousseau, M., 2019b - Paired-cosmogenic nuclides paleoaltimetry. Earth and Planetary Science Letters 515, 271-282.

Bosch, G.V., Teixell, A., Jolivet, M., Labaume, P., Stockli, D., Domènech, M., Monié, P., 2016. Timing of Eocene-Miocene thrust activity in the Western Axial Zone and Chaînons

Béarnais (west-central Pyrenees) revealed by multi-method thermochronology. Comptes Rendus Geoscience 348(3-4), 246-256. https://doi.org/10.1016/j.crte.2016.01.001

Bourdet, A., 2014. Datation des systèmes karstiques étagés et incision des vallées dans la moitié orientale des Pyrénées : le cas de l'Ariège dans la région de Tarascon (Master thesis), Université de Perpignan, Perpignan.

Braucher, R., Merchel, S., Borgomano, J., Bourlès, D.L., 2011. Production of cosmogenic radionuclides at great depth: a multi element approach. Earth and Planetary Science Letters 309, 1–9. https://doi.org/10.1016/j.epsl.2011.06.036

Brown, E.T., Edmond, J.M., Raisbeck, G.M., Yiou, F., Kurz, M.D., Brook, E.J., 1991. Examination of surface exposure ages of Antarctic moraines using in situ produced ^{10}Be and ^{26}Al. Geochimica et Cosmochimica Acta 55, 2269–2283. https://doi.org/10.1016/0016-7037(91)90103-C

Brown, E.T., Stallard, R.F., Larsen, M.C., Raisbeck, G.M., Yiou, F., 1995. Denudation rates determined from the accumulation of in situ-produced ^{10}Be in the luquillo experimental forest, Puerto Rico. Earth and Planetary Science Letters 129, 193–202. https://doi.org/10.1016/0012-821X(94)00249-X

Calvet, M., 1996. Morphogenèse d'une montagne méditerranéenne : les Pyrénées orientales. Documents du BRGM 255.

Calvet M., Gunnell Y., 2008. Planar landforms as markers of denudation chronology: an inversion of East Pyrenean tectonics based on landscape and sedimentary basin analysis. In: Gallagher K., Jones S.J., Wainwright J. (eds), Landscape Evolution: Denudation, Climate and Tectonics Over Different Time and Space Scales, Geological Society, London, Special Publications 296, 147–166. https://doi.org/10.1144/SP296.10

Chmeleff, J., von Blanckenburg, F., Kossert, K., Jakob, J., 2010. Determination of the ^{10}Be half-life by multicollector ICP-MS and liquid scintillation counting. Nuclear Instruments and Methods in Physics Research Section B 268, 192–199. https://doi.org/10.1016/j.nimb.2009.09.012

Choukroune, P., 1992. Tectonic evolution of the Pyrenees, Ann. Rev. Earth Planet. Sci. 20, 143. https://doi.org/10.1146/annurev.ea.20.0501192.001043

Crest, Y., Delmas, M., Braucher, R., Gunnell, Y., Calvet, M., ASTER Team., 2017. Cirques have growth spurts during deglacial and interglacial periods: Evidence from ^{10}Be and ^{26}Al nuclide inventories in the central and eastern Pyrenees. Geomorphology 278, 60-77. https://doi.org/10.1016/j.geomorph.2016.10.035

Crest, Y., 2017. Quantification de la dénudation glaciaire et postglaciaire dans l'orogène pyrénéen (PhD thesis). Université de Perpignan-Via-Domitia, Perpignan.

Delmas, M., 2009. Chronologie et impact géomorphologique des glaciations quaternaires dans l'est des Pyrénées (PhD thesis). Université Panthéon-Sorbonne - Paris I, Paris.

Delmas, M., Calvet, M., Gunnell, Y., Braucher, R., Bourlès, D. L., 2011. Palaeogeography and ^{10}Be exposure-age chronology of Middle and Late Pleistocene glacier systems in the northern Pyrenees: Implications for reconstructing regional palaeoclimates. Palaeogeography Palaeoclimatololgy Palaeoecology 305, 109–122. https://doi.org/10.1016/j.palaeo.2011.02.025

Delmas, M., Calvet, M., Gunnell, Y., Braucher, R., Bourlès, D. L., 2012. Les glaciations quaternaires dans les Pyrénées ariégeoises : approche historiographique, données paléogéographiques et chronologiques nouvelles. Quaternaire 23, 61–85. https://doi.org/10.4000/quaternaire.6091

Delmas, M., Braucher, R., Gunnell, Y., Guillou, V., Calvet, M., Bourlès, D.L. and ASTER Team., 2015. Constraints on Pleistocene glaciofluvial terrace age and related soil chronosequence features from vertical ^{10}Be profiles in the Ariège River catchment (Pyrenees, France). Global and Planetary Change 132, 39-53. https://doi.org/10.1016/j.gloplacha.2015.06.011

Denèle, Y., 2007. Formation des dômes gneissiques hercyniens dans les Pyrénées : exemple du massif de l'Aston-Hospitalet (PhD thesis). Université Toulouse-III–Paul Sabatier, Toulouse.

Dunai, T. J., 2010. Cosmogenic Nuclides, Principles, Concepts and Applications in the Earth Surface Sciences. Cambridge University Press, 198 pages; ISBN-13: 9780521873802

Engel, W., 1984. Migration of folding and flysch sedimentation on the southern flank of the Variscan belt (Montagne Noire, Mouthoumet massif, Pyrenees). Z. dt. Geol. Ges. 135, 279-292.

Fitzgerald, P.G., Muñoz, J.A., Coney, P.J., Baldwin, S.L., 1999. Asymmetric exhumation across the Pyrenean orogen: implications for the tectonic evolution of a collisional orogen. Earth and Planetary Science Letters 173, 157–170, https://doi.org/10.1016/S0012-821X(99)00225-3

Genti, M., 2015. Impact des processus de surface sur la déformation actuelle des Pyrénées et des Alpes (PhD thesis). Université de Montpellier, Montpellier.

Genti, M., Chery, J., Vernant, P., Rigo, A., 2015. Impact of gravity forces and topography denudation on normal faulting in Central–Western Pyrenees: Insights from 2D numerical models. Comptes Rendus Geoscience 348(3-4), 173-183. https://doi.org/10.1016/j.crte.2015.08.004

966 Goron, L., 1937. Les unités topographiques du Pays ariégeois : Le rôle des cycles d'érosion
967 tertiaires et des glaciations quaternaires dans leur morphologie. Revue géographique des
968 Pyrénées et du Sud-Ouest 8(4), 300-334. https://doi.org/10.3406/rgpso.1937.4268

969 Granger, D. E., & Muzikar, P. F., 2001. Dating sediment burial with in situ-produced
970 cosmogenic nuclides: Theory, techniques, and limitations. Earth Planet. Sci. Lett. 188, 269-
971 281. https://doi.org/10.1016/S0012-821X(01)00309-0

972 Granger, D. E., 2006. « A review of burial dating methods using ^{26}Al and ^{10}Be", In Situ-
973 Produced Cosmogenic Nuclides and Quantification of Geological Processes, Ana María
974 Alonso-Zarza, Lawrence H. Tanner. https://doi.org/10.1130/2006.2415(01)

975 Gunnell Y., Calvet M., Brichau S., Carter A., Aguilar J.P., Zeyen H., 2009. Low long-term
976 erosion rates in high energy mountain belts: insights from thermo- and biochronology in the
977 Eastern Pyrenees. Earth and Planetary Science Letters 278, 208-218.
978 https://doi.org/10.1016/j.epsl.2008.12.004

979 Haq, B.U., Hardenbol, J, Vail, P.R., 1987. Chronology of Fluctuating Sea Levels Since the
980 Triassic. Science 235, 1156-1167. https://doi.org/10.1126/science.235.4793.1156

981 Häuselmann, P., & Granger, D., 2005. Dating of caves by cosmogenic nuclides: Method,
982 possibilities, and the siebenhengste example (Switzerland). Acta Carsologica 34. 43-50.
983 10.3986/ac.v34i1.278.

984 Häuselmann, P., 2007. How to date nothing with cosmogenic nuclides. Acta Carsologica,
985 Time in Karst, Potstojna 36(1), 93-100. http://dx.doi.org/10.3986/ac.v36i1.212

986 Häuselmann, P., & Mihevc, A., Pruner, P., Horacek, I., Cermak, S., Hercman, H., Sahy, D.,
987 Fiebig, M., Hajna, N., Bosak, P., 2015. Snežna jama (Slovenia): Interdisciplinary dating of
988 cave sediments and implication for landscape evolution. Geomorphology 247. 10-24.
989 10.1016/j.geomorph.2014.12.034.

990 Häuselmann, P., Plan, L., Pointner, P., Fiebig, M., 2020. Cosmogenic nuclide dating of cave
991 sediments in the Eastern Alps and implications for erosion rates. International Journal of
992 Speleology 49, 107-118. 10.5038/1827-806X.49.2.2303.

993 Herman, F., Seward, D., Valla, P.G., Carter, A., Kohn, B., Wilett, S.D., Ehlers, T.A., 2013.
994 Worldwide acceleration of mountain erosion under a cooling climate. Nature 504(7480), 423-
995 426. doi:10.1038/nature12877

996 Honda, M., Zhang, X., Phillips, D., Hamilton, D., Deerberg, M., Schwieters, J.B., 2015.
997 Redetermination of the ^{21}Ne relative abundance of the atmosphere, using a high resolution,
998 multi-collector noble gas mass spectrometer (HELIX-MC Plus). International Journal of Mass
999 Spectrometry 387, 1–7. https://doi.org/10.1016/j.ijms.2015.05.012

1000 Jolivet, M., Labaume, P., Monié, P., Brunel, M., Arnaud, N., Campani, M., 2007.
1001 Thermochronology constraints for the propagation sequence of the South Pyrenean basement
1002 thrust system (France–Spain). Tectonics 26, TC5007,
1003 http://dx.doi.org/10.1029/2006TC002080.

1004 Kober, F., Ivy-Ochs, S., Schlunegger, F., Baur, H., Kubik, P.W., Wieler, R., 2007.
1005 Denudation rates and a topography-driven rainfall threshold in northern Chile: Multiple
1006 cosmogenic nuclide data and sediment yield budgets. Geomorphology 83, 97-120.
1007 https://doi.org/10.1016/j.geomorph.2006.06.029

1008 Korschinek, G., Bergmaier, A., Faestermann, T., Gerstmann, U.C., Knie, K., Rugel,
1009 G.,Wallner, A., Dillmann, I., Dollinger, G., von Gostomski, Lierse Ch., Kossert, K.,
1010 Maitia,M., Poutivtsev, M., Remmert, A., 2010. A new value for the half-life of ^{10}Be by
1011 Heavy-Ion Elastic Recoil Detection and liquid scintillation counting. Nuclear Instruments and
1012 Methods in Physics Research Section B 268, 187–191.
1013 https://doi.org/10.1016/j.nimb.2009.09.020

1014 Labaume, P., Meresse, F., Jolivet, M., and Teixell, A., 2016. Exhumation sequence of the
1015 basement thrust units in the west-central Pyrenees. Constraints from apatite fission track
1016 analysis. Geogaceta 60, 11-14.

1017 Lagabrielle, Y., Labaume, P. and de Saint Blanquat, M., 2010. Mantle exhumation, crustal
1018 denudation, and gravity tectonics during Cretaceous rifting in the Pyrenean realm (SW
1019 Europe): Insights from the geological setting of the lherzolite bodies. Tectonics 29(4),
1020 TC4012, https://doi.org/10.1029/2009TC002588.

1021 Lagasquié, J., 1963. Le relief calcaire du plateau de Sault. Revue Géographique des Pyrénées
1022 et du Sud-Ouest 34, 11-32. https://doi.org/10.3406/rgpso.1963.4753

1023 Lal, D. 1991. Cosmic ray labeling of erosion surfaces: in situ nuclide production rates and
1024 erosion models. Earth and Planetary Science Letters 104(2-4), 424-439.
1025 https://doi.org/10.1016/0012-821X(91)90220-C

1026 Laureano, F.V., Karmann, I., Granger, D.E., Auler, A.S., Almeida, R.P., Cruz, F.W., Strícks,
1027 N.M., and Novello, V.F., 2016. Two million years of river and cave aggradation in NE Brazil:
1028 Implications for speleogenesis and landscape evolution. Geomorphology 273, 63-77.
1029 https://doi.org/10.1016/j.geomorph.2016.08.009

1030 Martin, L.C.P, Blard, P.-H., Balco, G., Lavé, J., Delunel, R., Lifton, N., Laurent, V., 2017.
1031 The CREp program and the ICE-D production rate calibration database: A fully
1032 parameterizable and updated online tool to compute cosmic-ray exposure ages. Quaternary
1033 Geochronology 38, 25-49. https://doi.org/10.1016/j.quageo.2016.11.006

1034 Maurel, O., Monié, P., Pik, R., Arnaud, N., Brunel, M., Jolivet, M., 2008. The Meso-
1035 Cenozoic thermo-tectonic evolution of the Eastern Pyrenees: An Ar-40/Ar-39 fission track
1036 and (U-Th)/He thermochronological study of the Canigou and Mont-Louis Massifs.

International Journal of Earth Sciences 97. 565-584. https://doi.org/10.1007/s00531-007-0179-x.

Merchel, S., Herpers, U., 1999. An update on radiochemical separation techniques for the determination of long-lived radionuclides via accelerator mass spectrometry. Radiochimica Acta 84, 215–219. https://doi.org/10.1524/ract.1999.84.4.215

Merchel, S., Bremser, W., 2004. First international 26Al interlaboratory comparison – Part I. Nuclear Instrumentation Methods in Physics Research, Section B: Beam Interactions with Materials and Atoms 223–224, 393–400. https://doi.org/10.1016/j.nimb.2005.05.051

Merchel, S, Arnold, M., Aumaître, G., Benedetti,L., Bourlès, D.L., Braucher, R., Alfimov, V., Freeman, S.P.H.T, and Wallner, A., 2008. Towards more precise ^{10}Be and ^{36}Cl data from measurements at the 10^{-14} level: Influence of sample preparation. Nuclear Instruments and Methods in Physics Research B 266, 4921–4926. https://doi.org/10.1016/j.nimb.2008.07.031

Milesi, G., Monié, P., Soliva, R., Münch, P., Taillefer, A., Bellanger, M., Brugnier, O., Bonno, M., Martin, C., 2020. Imaging Geothermal Anomalies Using Low-temperature (U-Th)/He Thermochronometry: A Case Study from the Active Têt Fault Hydrothermal System (Eastern Pyrenees, France). Proceedings World Geothermal Congress 2020 Reykjavik, Iceland, April 26 – May 2, 2020

Mocochain, L., Audra, P., Clauzon, G., Bellier, O., Bigot, J.-Y., Parize, O., Monteil, P., 2009. The effect of river dynamics induced by the Messinian Salinity Crisis on karst landscape and caves: Example of the Lower Ardèche river (mid Rhône valley). Geomorphology 106, 46–61. https://doi.org/10.1016/j.geomorph.2008.09.021

Molliex, S., Rabineau, M., Lerouxv E., Bourlès, D.L., Authemayou, C., Aslanian, D., Chauvet, F., Cive,t F., Jouët, G., 2016. Multi-approach quantification of denudation rates in the Gulf of Lion source-to-sink system (SE France). Earth and Planetary Science Letters 444, 101-115. https://doi.org/10.1016/j.epsl.2016.03.043

Molnar, P., 2004. Late Cenozoic increase in accumulation rates of terrestrial sediment: how might climate change have affected erosion rates? Annu. Rev. Earth Planet. Sci. 32, 67–89. https://doi.org/10.1146/annurev.earth.32.091003.143456.

Monod, B., Allanic, C., Bailly-Comte, V., Jacob, T., avec la collaboration de Martel, L., Courrioux, G., 2016a. Évaluation des ressource en eaux souterraines du Plateau de Sault – étude structurale, modèle géologique 3D, acquisition gravimétrique et analyse de la fracturation, Rapport final BRGM/RP-68288-FR, 155 p., 91 ill., 1 tabl., 2 annexes

Monod, B., Regard, V., Carcone, J., Wyns, R. and Christophoul, F., 2016b. Postorogenic planar palaeosurfaces of the central Pyrenees: Weathering and neotectonic records. Comptes Rendus Geoscience 348(3-4), 184-193, https://doi.org/10.1016/j.crte.2015.09.005

Morris, R.G., Sinclair, H.D., Yelland, A.J., 1998. Exhumation of the Pyrenean orogen: implications for sediment discharge. Basin Research 10, 69–85, http://dx.doi.org/10.1046/j.1365-2117.1998.00053.x.

Mouchené, M., van der Beek, P., Mouthereau, F., Carcaillet, J., 2017. Controls on Quaternary incision of the Northern Pyrenean foreland: Chronological and geomorphological constraints from the Lannemezan megafan, SW France. Geomorphology 281, 78-93. https://doi.org/10.1016/j.geomorph.2016.12.027

Niedermann, S., 2002. Cosmic-ray-produced noble gases in terrestrial rocks: dating tools for surface processes. In: Porcelli, D., Ballentine, C., Wieler, R. (Eds.), Noble gases in geochemistry and cosmochemistry. Vol. 47 of Reviews in Mineralogy and Geochemistry. Mineralogical Society of America, pp. 731–784.

Nishiizumi, K.; Imamura, M.; Caffee, M.W.; Southon, J.R.; Finkel, R.C.; McAninch, J., 2007. Absolute calibration of ^{10}Be AMS standards. Nuclear Instrumentation Methods in Physics Research, Section B 258, 403–413. https://doi.org/10.1016/j.nimb.2007.01.297

Nivière, B., Lacan, P., Regard, V., Delmas, M., Calvet, M., Huyghe, D., Roddaz, B., 2016. Evolution of the Late Pleistocene Aspe River (Western Pyrenees, France). Signature of climatic events and active tectonics. Comptes Rendus Geoscience 348(3-4), 203-212. https://doi.org/10.1016/j.crte.2015.07.003

Olivetti, V., Godard, V., Bellier, O., ASTER Team., 2016. Cenozoic rejuvenation events of Massif Central topography (France): Insights from cosmogenic denudation rates and river profiles. Earth and Planetary Science Letters 444, 179-191. https://doi.org/10.1016/j.epsl.2016.03.049

Plan, L., Filipponi, M., Behm, M., Seebacher, R., Jeutter, P., 2009. Constraints on alpine speleogenesis from cave morphology – A case study from the eastern Totes Gebirge (Northern Calcareous Alps, Austria). Geomorphology 118-129. https://doi.org/10.1016/j.geomorph.2008.09.011

Puchol, N., Lavé, J., Lupker, M., Blard, P.-H., Gallo, F., France-Lanord, C., ASTER Team., 2014. Grain-size dependent concentration of cosmogenic 10Be and erosion dynamics in a landslide-dominated Himalayan watershed. Geomorphology 224, 55-68. https://doi.org/10.1016/j.geomorph.2014.06.019

Puchol, N., Charreau, J., Blard, P.-H., Lavé, J., Dominguez, S., Pik, R., Saint-Carlier, D., ASTER Team., 2017. Limited impact of Quatrenary glaciations on denudation rates in Central Asia. Geological Society of America Bulletin 129 (3-4), 479-499. https://doi.org/10.1130/B31475.1

Samworth, E.A., Warburton, E.K., Engelbertink, G.A.P., 1972. Beta decay of the ^{26}Al ground state. Physical Review C5, 138-142.

Sartégou, A., 2017. Évolution morphogénique des Pyrénées orientales : apports des datations de systèmes karstiques étagés par les nucléides cosmogéniques et la RPE. Université de Perpignan Via-Domitia, Perpignan (In French and results in English). https://tel.archives-ouvertes.fr/tel-01708921

Sartégou, A., Bourlès, D.L., Blard, P.-H., Braucher, R., Tibari, B., Zimmermann, L., Leanni, L. and ASTER Team., 2018. Deciphering landscape evolution with karstic networks: A Pyrenean case study. Quaternary Geochronology 43, 12 - 29. https://doi.org/10.1016/j.quageo.2017.09.005

Shuster, David L. and Farley, Kenneth A. 2005., Diffusion kinetics of proton-induced ^{21}Ne, ^{3}He, and ^{4}He in quartz. Geochimica et Cosmochimica Acta 69 (9), 2349-2359. ISSN 0016-7037

Sinclair, H.D., Gibson, M., Naylor, M., Morris, R.G., 2005. Asymmetric growth of the Pyrenees revealed through measurement and modeling of orogenic fluxes. American Journal of Science 305, 369–406, http://dx.doi.org/10.2475/ ajs.305.5.369.

Sorriaux, P., 1981. Étude et datation de remplissages karstiques : nouvelles données sur la paléogéographie quaternaire de la région de Tarascon (Pyrénées ariégeoises). C.R. Acad. Sc. Paris 293, Série II – 703. In French.

Sorriaux, P., 1982. Contribution à l'étude de la sédimentation en milieu karstique. Le système de Niaux – Lombrives – Sabart (Pyrénées ariégeoises) (PhD thesis) Université Paul Sabatier, Toulouse.

Sorriaux, P., Delmas, M., Calvet, M., Gunnell, Y., Durand, N., and Pons-Branchu, E., 2016. Relations entre karst et glaciers depuis 450 ka dans les grottes de Niaux-Lombrives-Sabart (Pyrénées ariégeoises). Nouvelles datations U/Th dans la grotte de Niaux. Karstologia.

Stange, K.M., van Balen, R.T., Kasse, C., Vandenberghe J., Carcaillet, J., 2014. Linkin g morphology across glaciofluvial interface: A ^{10}Be supported chronology of glacier advanced and terrace formation in the Garonne River, northern Pyrenees, France. Geomorphology 207, 71-95. https://doi.org/10.1016/j.geomorph.2013.10.028

Stange, K.M., van Balen, R.T., Carcaillet, J. & Vandenberghe J., 2013. Terrace staircase development in the Southern Pyrenees Foreland: Inferences from ^{10}Be terrace exposure ages at the Segre River. Global and Planetary Change 101, 97-112. https://doi.org/10.1016/j.gloplacha.2012.12.007

Stange, K.M., van Balen, R.T., Vandenberghe J., Peña, J.-L. & Sancho, C., 2012. External controls on Quaternary fluvial incision and terrace formation at the Segre River, Southern Pyrenees. Tectonophysics 602, 313-331. https://doi.org/10.1016/j.tecto.2012.10.033

Stone, J.O., 2000. Air pressure and cosmogenic isotope production. Journal of geophysical Research : Solid Earth 105(B10), 23753-23759. https://doi.org/10.1029/2000JB900181

Vacherat, A., Mouthereau, F., Pik, R., Bellahsen, N., Gautheron, C., Bernet, M., Daudet, M., Balansa, J., Tibari, B., Jamme, R.P. and Radal, J., 2016. Rift-to-collision transition recorded by tectonothermal evolution of the northern Pyrenees. Tectonics 35(4), 905-933. https://doi.org/10.1002/2015TC004016

Vermeesch, P., Balco, G., Blard, P.-H., Dunai, T.J., Kober, F., Niedermann, S., Shuster, D.L., Strasky, S., Finlay, F.M., Wieler, R. & Zimmermann, L., 2015. Interlaboratory comparison of cosmogenic ^{21}Ne in quartz. Quaternary Geochronology 26, 20-28. https://doi.org/10.1016/j.quageo.2012.11.009

Zimmermann, L., Füri, E. & Burnard, P., 2015. Purification des gaz rares sous ultravide – Méthodes de purification. Techniques de l'Ingénieur – Fabrication des grands produits industriels en chimie et pétrochimie, J 6635, 17 pp.

Zimmermann, L., Avice, G., Blard, P.-H., Marty, B., Füri, E., and Burnard, P.G., 2018. A new all-metal induction furnace for noble gas extraction. Chemical Geology 480, 86-92. https://doi.org/10.1016/j.chemgeo.2017.09.018

Figures

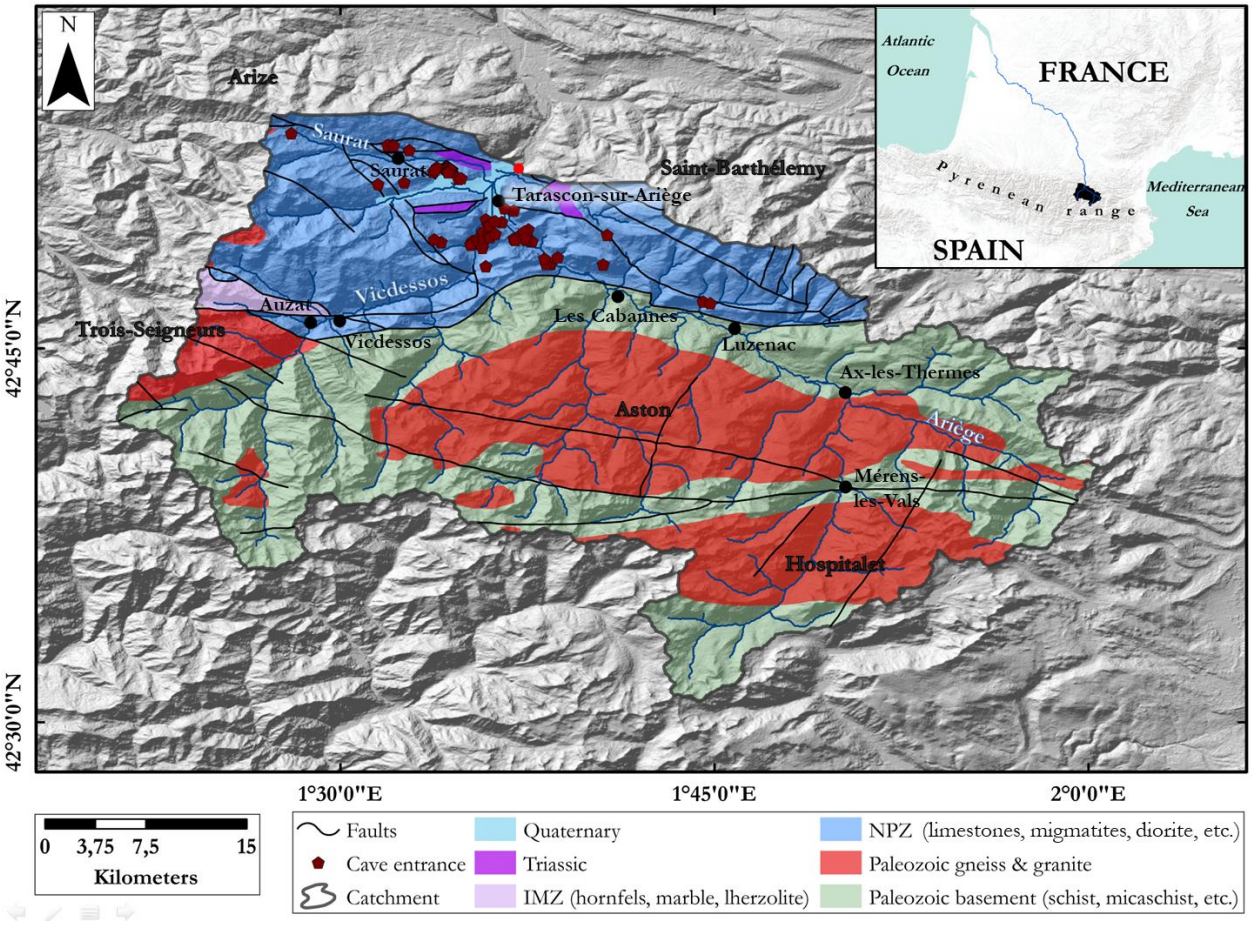

Fig. 1. Lithostructural features of the Ariège catchment (based on IGME-BRGM data). Alluvial sediments trapped in karstic networks originated from Palaeozoic crystalline massifs (gneisses, granites, and metasediments) before joining the limestones of the North-Pyrenean zone (NPZ) or from the varied lithologies of the internal metamorphic zone (IMZ). The area is tectonically complex, and the Cretaceous limestone cliffs of the NPZ are dotted with caves that served as shelters during prehistoric times and during religious wars. The watershed also includes glacial deposits at high altitudes.

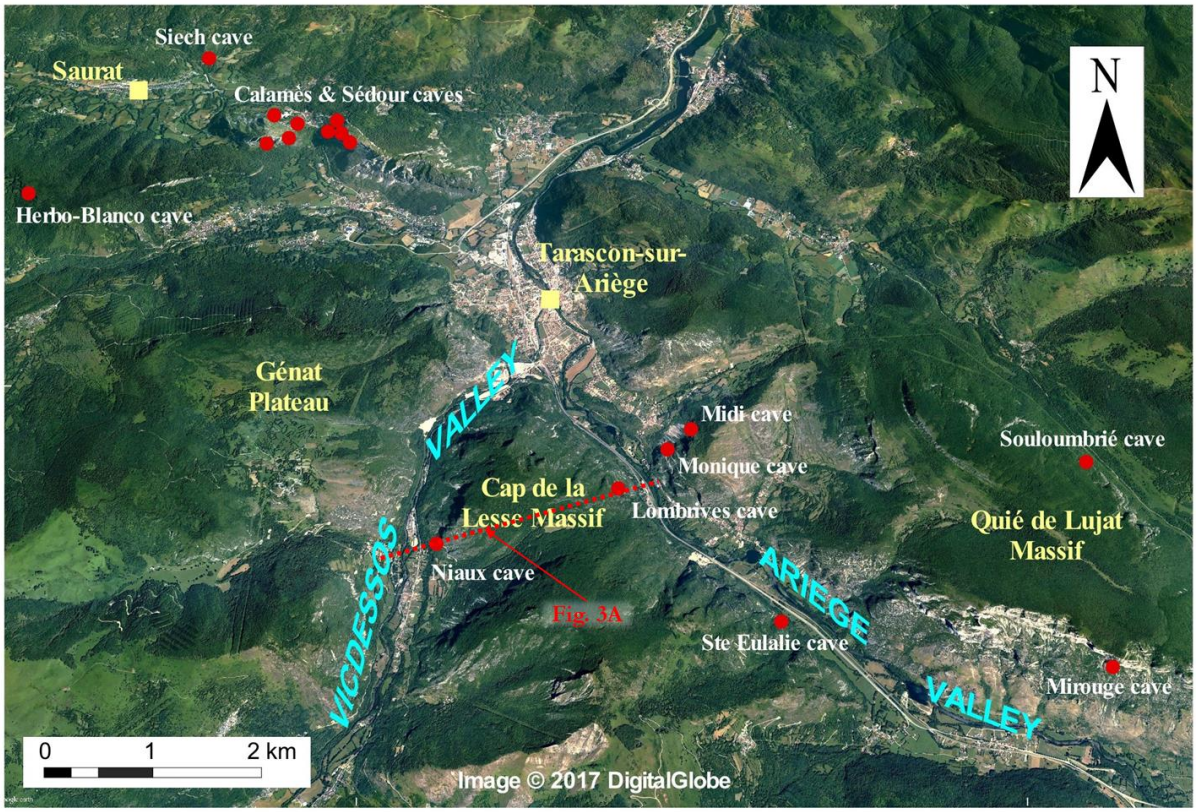

Fig. 2. The Ariège River valley near Tarascon-sur-Ariège, highlighting the spatial distribution of the karstic network within the massifs. Epiphreatic levels are identifiable at the Quié de Lujat (east bank), Cap de la Lesse (Fig. 3), Calamès (Fig. 5), and Sédour (Fig. 4) massifs (west bank). These karstic networks developed due to variations in the levels of the Ariège River and its tributaries, the Vicdessos and Saurat Rivers. The perched levels have probably been trimmed over time by the removal of the flanks of the massifs.

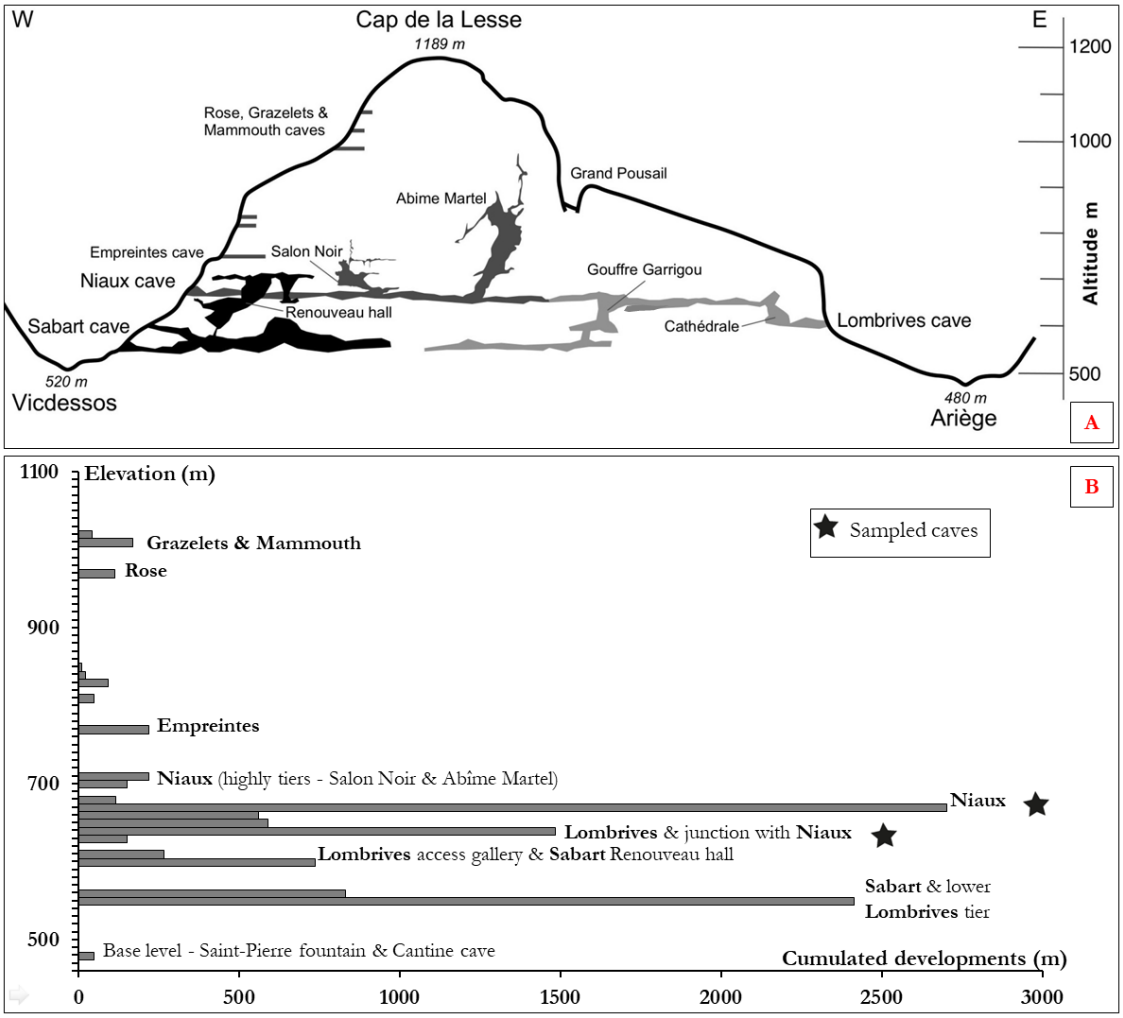

Fig. 3. Upper part (A) - Schematic cross-section of Cap de la Lesse massif (see Fig. 2 for location), showing the spatial distribution of the karstic network. Lower part (B) - Eight epiphreatic levels are identifiable, and some galleries are vertically connected. This network developed from the Ariège and Vicdessos Rivers. The floors linked to the Niaux-Lombrives-Sabart network are the most developed (altitudinal distribution shown at bottom) and are linked by a vertically branching network that does not originate from the surface. Perched levels were probably trimmed over time due to the removal of the flanks of the massif.

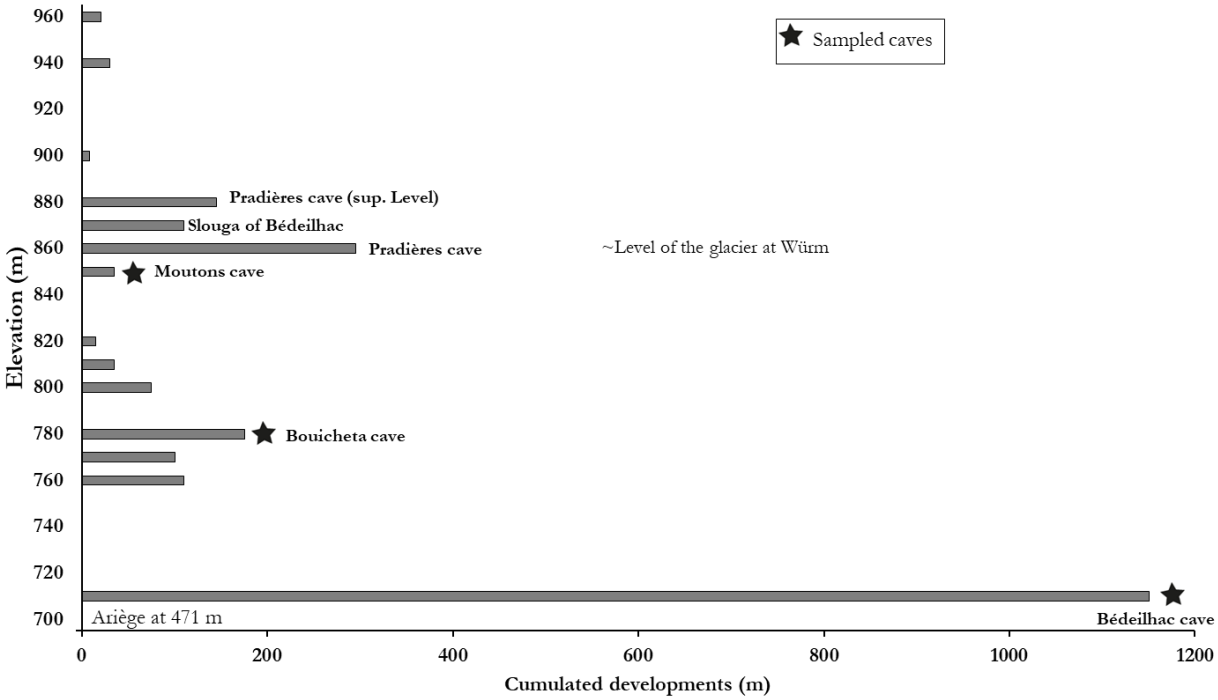

Fig. 4. Altitudinal distribution of caves of the Sédour massif. At least six epiphreatic levels are identifiable, which formed from the Saurat River, an Ariège River tributary. The Bédeilhac floor is the most developed (due to its significant length, it is not fully represented). Perched levels were probably rimmed over time due to the removal of the flanks of the massif.

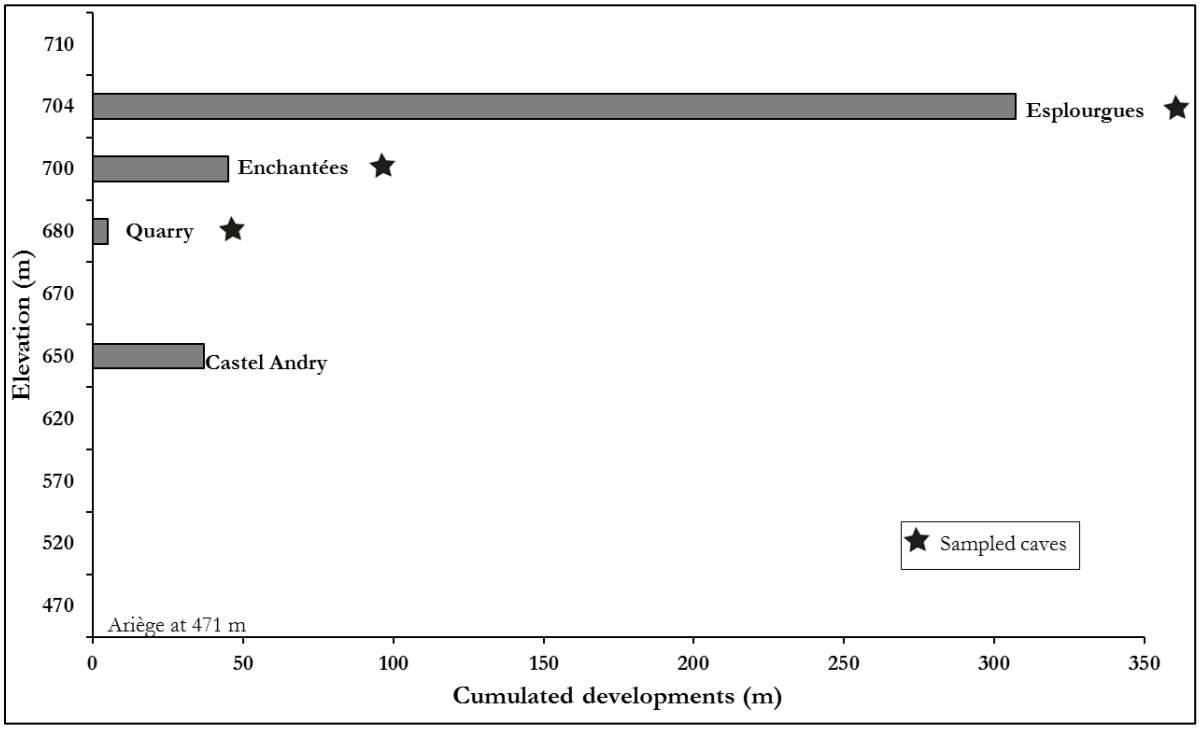

Fig. 5. Altitudinal distribution of caves of the Calamès massif. At least four epiphreatic levels are identifiable, which formed from the Saurat River, an Ariège tributary. This massif has been prospected by archaeologists. Perched levels were probably trimmed over time due to the removal of the flanks of the massif.

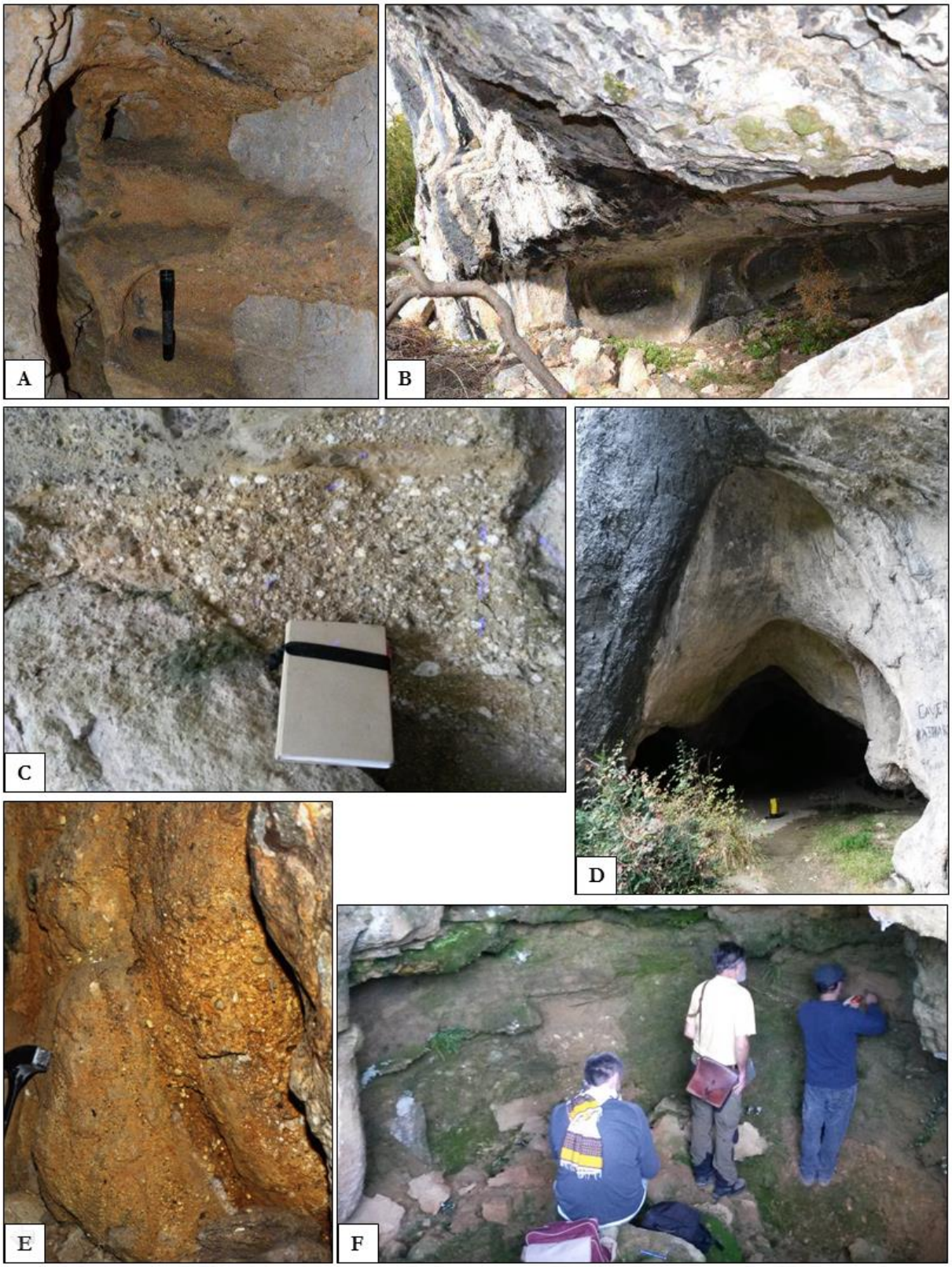

Fig. 6. A) Well consolidated sandstone plating along the wall of the Bouicheta cave. (B) The entrance to Moutons cave: convectional niches and remnants of stalagmitic floors are visible. (C) The alluvial deposits near an entrance to the Esplourgues cave. These highly altered coarse to pebbly deposits are part of a stratigraphic sequence that includes well consolidated clayey sands. These deposits indicate an insertion and contain fluid escape structures. (D) An entrances to the Esplourgues cave, showing large niches. (E) Very coarse, rubified, and highly altered sandy deposits cemented along the wall of

the Mirouge cave, in Quié de Lujat massif. (ph. By M. Nicol). (F) Sampling of medium-sand levels of the Quarry cave stratigraphic sequence. Below these sandy deposits are altered heterometric pebbles.

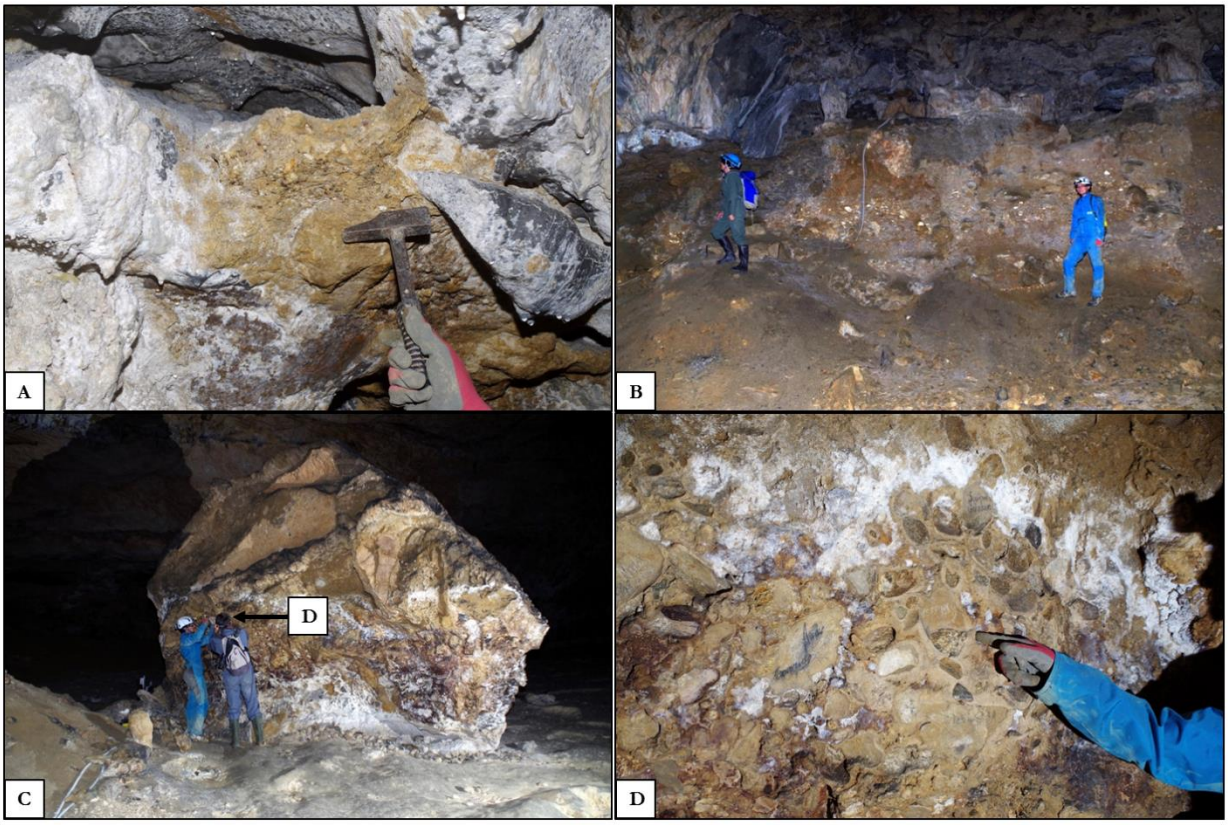

Fig. 7. Sampling in the Bédeilhac cave (ph. Sorriaux). (A) Deposits of medium to coarse sands on the wall of the Vidal gallery. (B) A section of the entry room in which a World War II aircraft hangar was installed. The thick alluvial deposits reflect high energy currents. Pebbles are altered and the deposits are rubified. (C) Collapsed stalagmitic pillar ("Tomb of Roland"). This large column has been displaced by currents and is probably very strong, as shown by its surface morphologies. (D) Granitic pebbles and medium to coarse sands are cemented at the base of the Tomb of Roland pillar.

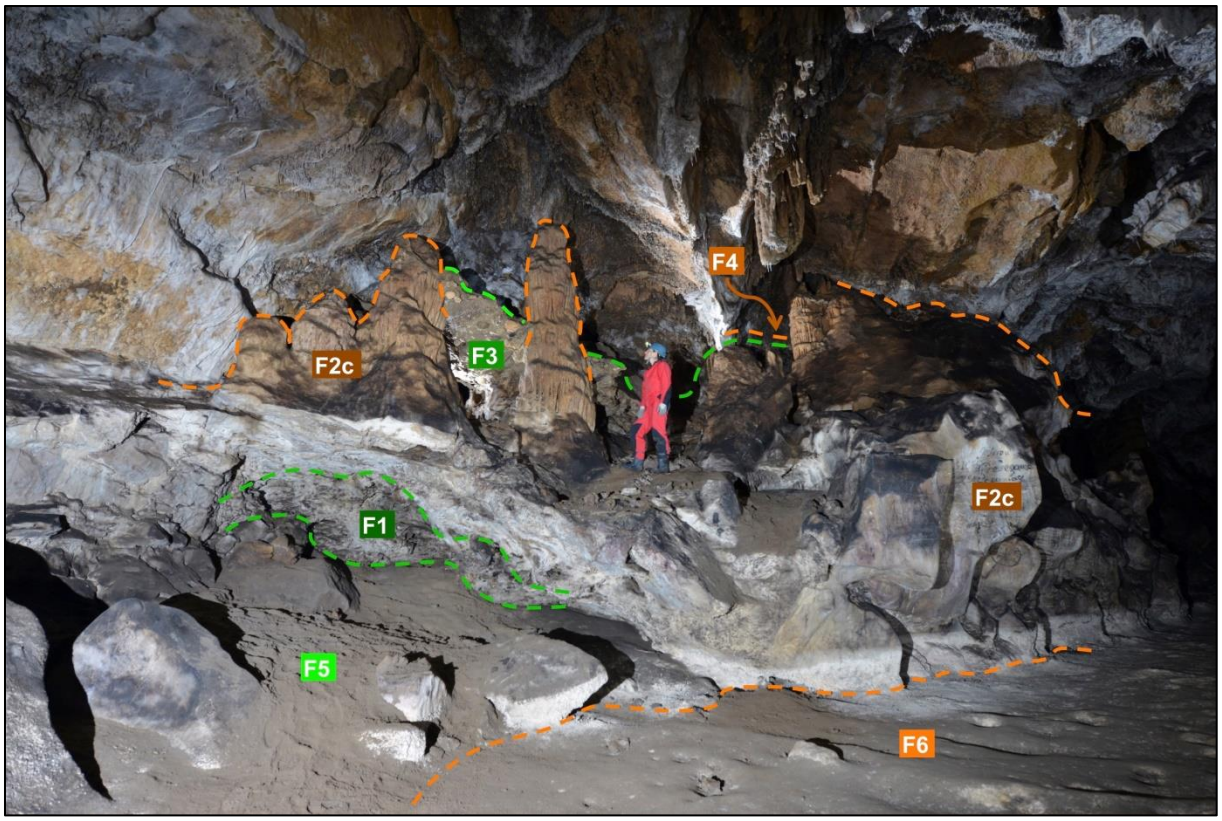

Fig. 8. Three successive sedimentary deposits were investigated in the Niaux and Lombrives caves (ph. P. Sorriaux and V. Guinot). Each deposit comprises two units: the lower units are detritic and of alluvial origin, and thus indicate the hydrology of the network, whereas the upper units mainly comprise calcitic deposits corresponding to drying periods when the karst evolved above the base level. These conditions are similar to the present-day cave environment. Some stalagmitic floors have been U-Th dated (Sorriaux, 1981; 1982; Bakalowicz et al., 1984). This reference outcrop is in Niaux cave, a few hundred meters from the entrance at approximately 670 m a.s.l. F1 is the oldest alluvial conglomerate; it includes a calcitic deposit (F2c) with two stalagmitic pillars, the oldest parts of which are older than 350 ka. The basic stalagmite floor (F2c) can have a thickness of several meters slightly further into the gallery. The tops of the pillars are covered by an alluvial conglomerate (F3) that is sealed behind the left pillar by a stalagmitic floor (F4) and is not visible on the photograph, which formed between 200 and 90 ka. Conglomerate F3 corresponds to a pre-Würm glacial phase, which is poorly known at the surface (Sorriaux et al., in press). The sands (F5) at the bottom of the photo are of fluvio-glacial origin corresponding to the Würm major glacial phase (90–20 ka), which reactivated the karst. Here, the sands are covered by clayey-calcitic sediments (F6) corresponding to the current drainage period.

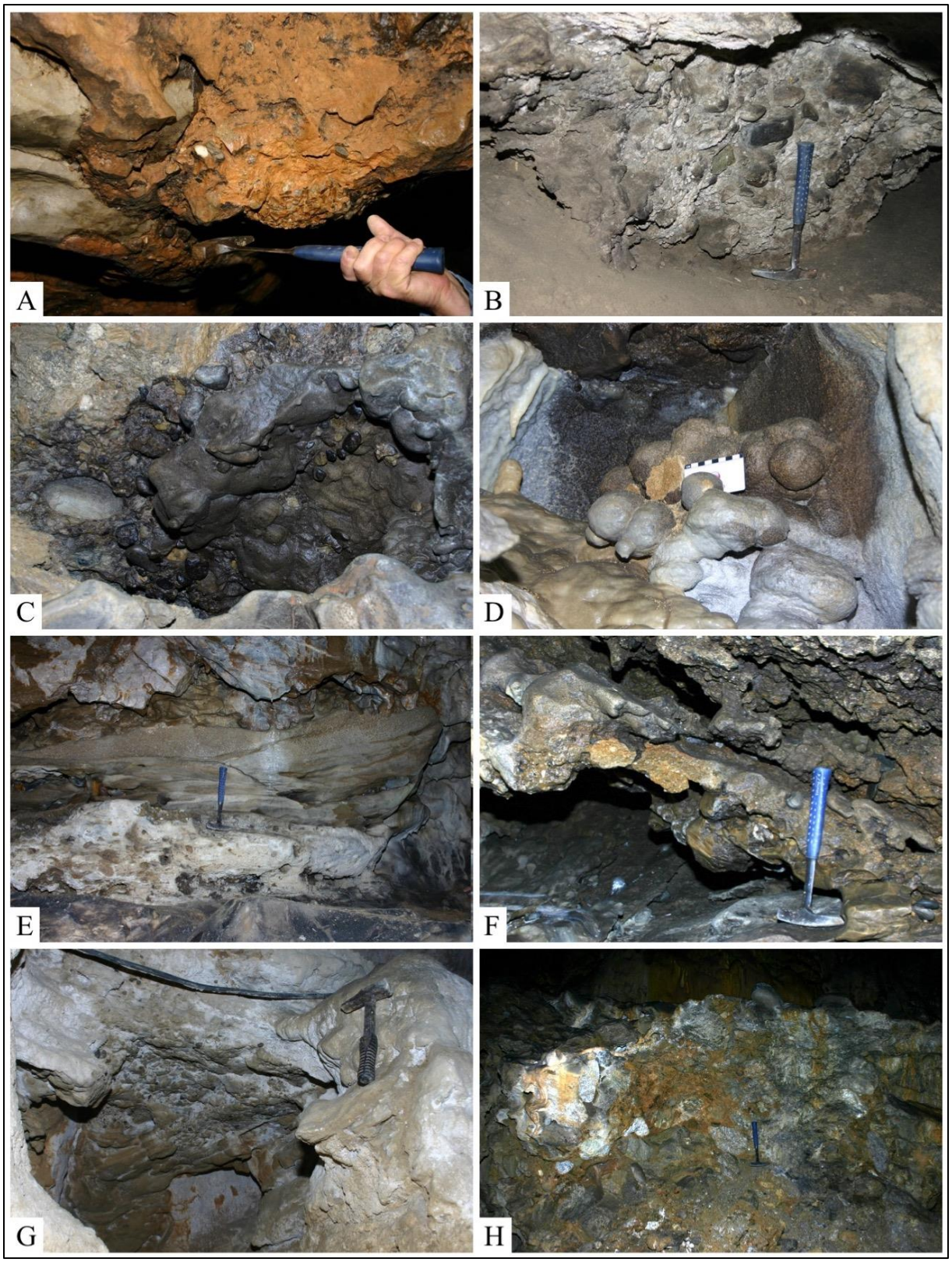

Fig. 9. Photographs of some of the Niaux and the Lombrives cave sampling sites. The F1 and F3 formations are described in the text after Sorriaux (1982). All photos are from P. Sorriaux. (A) Site Ni13-05. (B) Site Ni13-17. (C) Site LO5 at the *Salines* location. This conglomerate is part of the F1 alluvial formation. (D) Site LO3 at the entrance of the Vierge gallery. A soutirage of the shaft is observed at this site. Medium to coarse grained sandstone balls are highly concreted. These intergranular concretions typically formed in drowned passages, not very far below the water table (shallow sumps), in which flooding was only occasional (allowing sufficient time for these sands to

partly solidify). (E) Site LO7 near the Akka underground lake. The F3 alluvial formation (comprising conglomerates surmounted by coarse- to fine-grained sandstones) seals a red clay deposit. This sampling point clearly illustrates a channel morphology. (F) Site LO6 near Akka Lake. This F1 conglomerate is a well-consolidated conglomerate comprising gravel and crystalline pebbles in a sandy matrix. (G) Site LO8 in the Mamelle gallery. The sample was taken from a small niche to the left of the photograph. The material is very fine grained and hardened. Balls are noticeably altered, and a well-indurated coarser level seals this deposit. (H) Site LO2 in the Grand Chaos room. This formation includes highly weathered granitic pebbles in a fine to medium sand matrix. A floor seals this formation, into which blocks of unaltered granites are inserted.

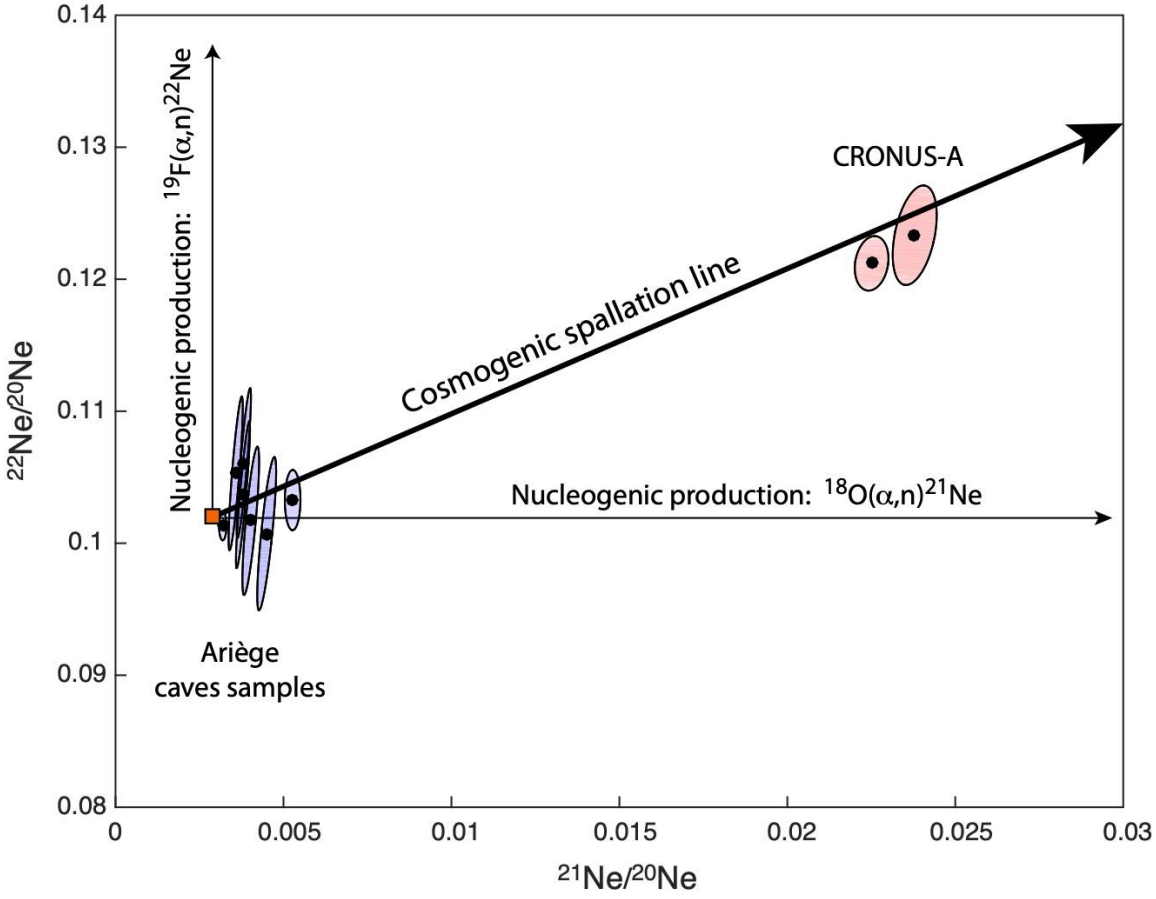

Fig. 10. Neon three-isotope diagram of quartz samples from caves of the Ariège River catchment. Most data from the Ariège samples (blue ellipses) are compatible with the atmosphere-spallation mixing line, similar to the CRONUS-A quartz standards (red ellipses).

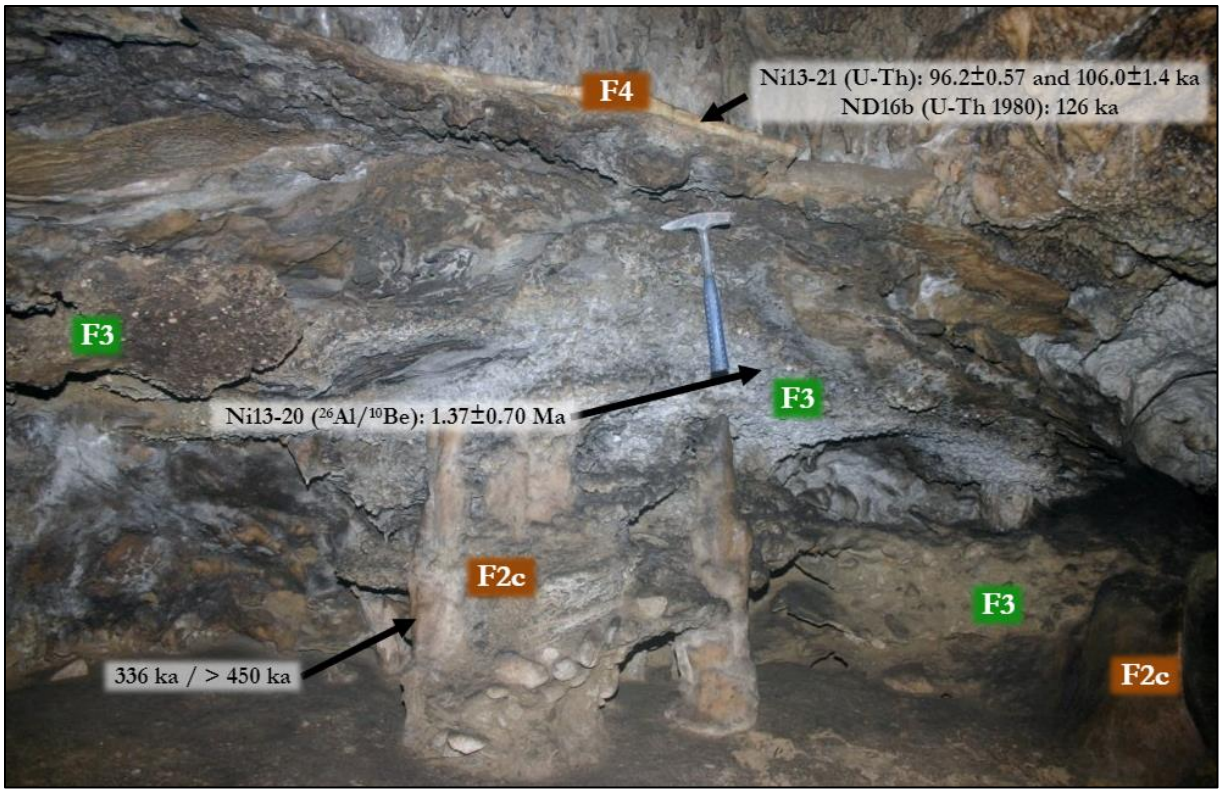

Fig. 11. A representative photograph of polyphased fillings in Niaux cave. The F3 sandstones are sealed by stalagmitic floors dated between ~150 and ~90 ka (Ni13-21; Sorriaux et al., 2016). The roof of the calcite complex (F2c) is older than c. 336 ka outside the concretion and ~450 ka (minimum ages) at the centre of the concretion (Ni13-18; Sorriaux et al., 2016). The F3 Formation yields heterogeneous burial durations (see Ni13-15, Ni13-20, and Ni13-23, Table 3).

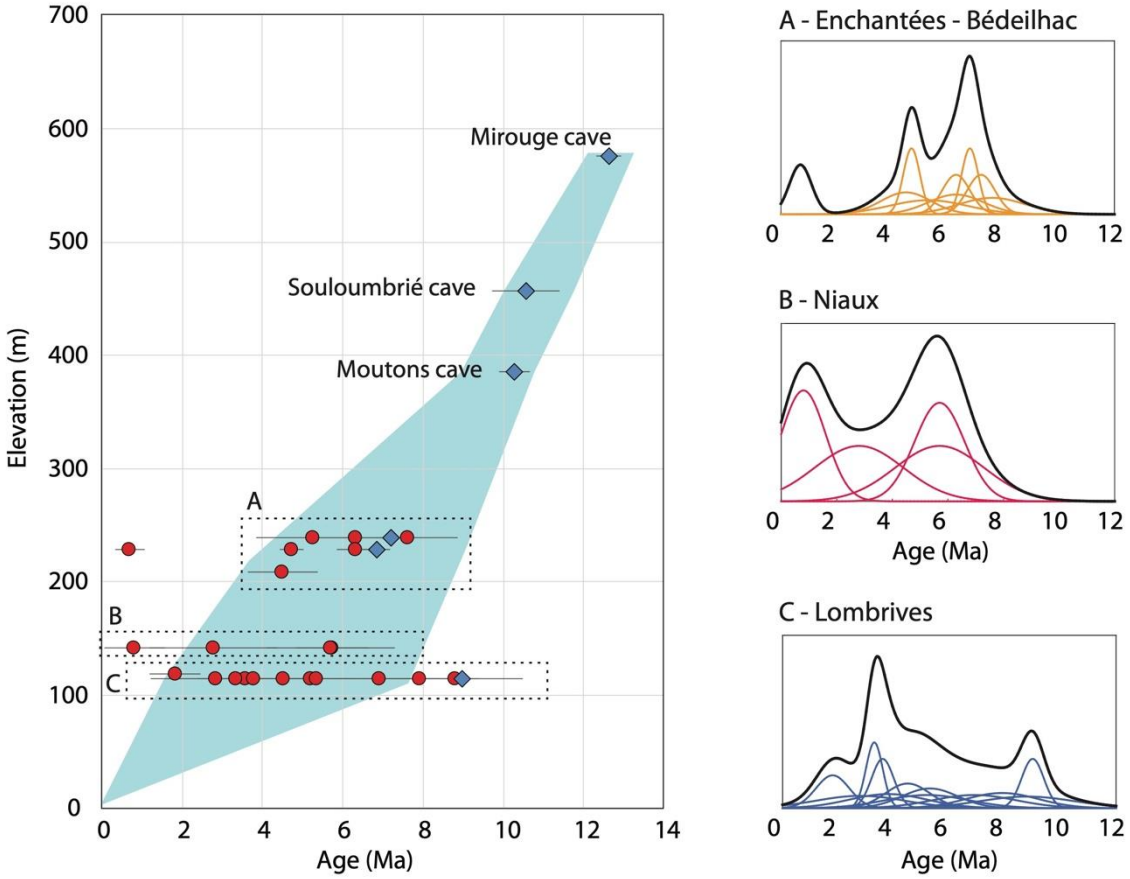

Fig. 12. Elevation vs. filling age of the Ariège karstic networks since 14 Ma (Langhian). Burial durations were determined from the $^{26}Al/^{10}Be$ (red dots) and $^{10}Be/^{21}Ne$ ratios (blue diamonds) of detrital sediments filling the caves. Burial durations were discarded for poorly purified samples containing residual muscovite. Small variations in the relative altitudes, related to gaps in the networks, are not represented in this plot. (A–C) Burial age distributions of samples from the Enchantées-Bédeilhac, Niaux, and Lombrives caves, respectively.

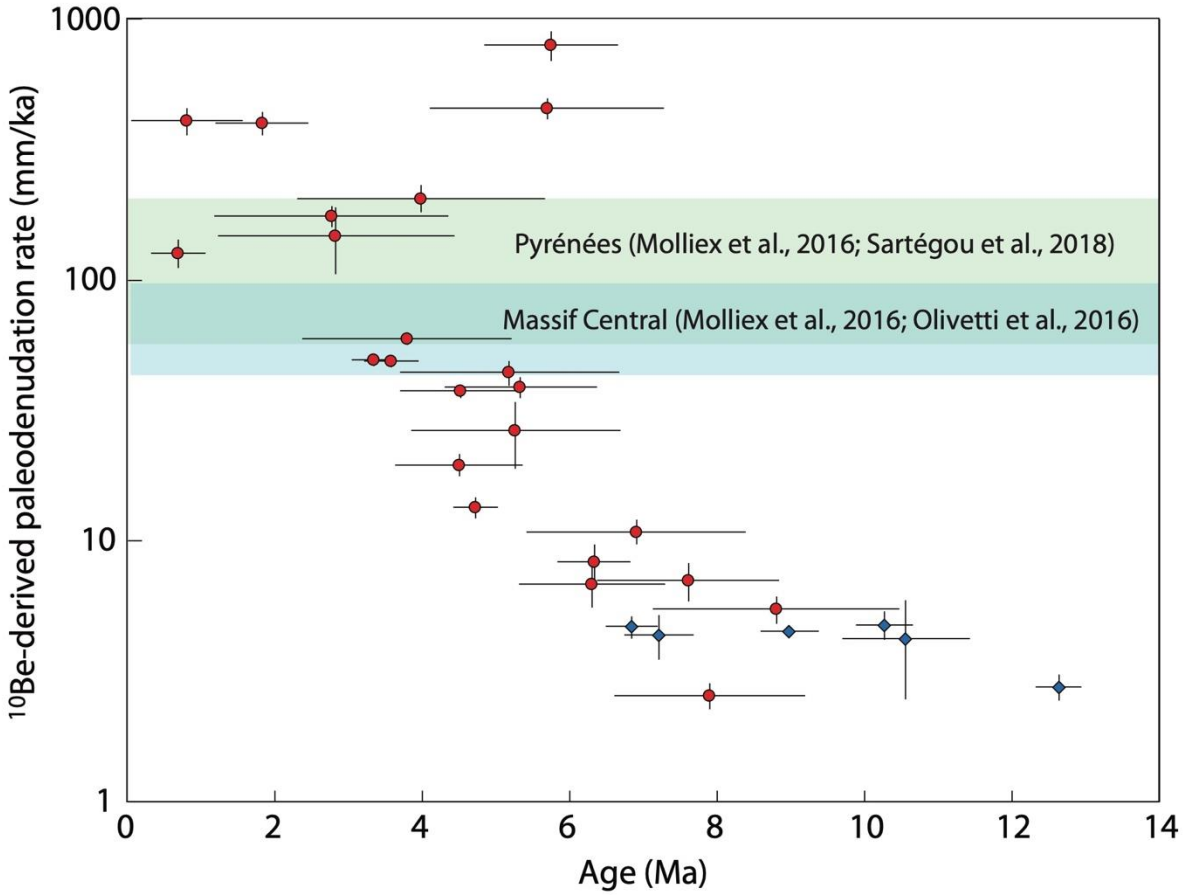

Fig. 13. ^{10}Be-derived palaeodenudation rates vs. filling age in the Ariège watershed since 14 Ma (Langhian). ^{10}Be concentrations are corrected for radioactive decay. Blue dots were obtained from samples analyzed for ^{21}Ne. The red dots were obtained from samples analyzed for ^{26}Al. Modern ^{10}Be palaeodenudation rates were obtained from modern river sands in the Pyrenees and Massif Central (Molliex et al., 2016; Olivetti et al., 2016; Sartégou et al., 2018).

Tables

Massif	Cave	Cave ID	Latitude (°)	Longitude (°)	Elevation (m a.s.l.)	Relative elevation (m)	Length (m)
Cap de la Lesse	Sainte-Eulalie	ASAR115	42.809997	1.636363	570	20	62
	Lombrives network	ASAR110	42.823389	1.616056	605	114	7000
	Tunnel Lombrives	ASAR111	42.823547	1.615785	610	119	19
	Niaux network	ABOU101	42.819667	1.593750	672	142	4000
Sédour - Calamès	Bédeilhac Quarry	ASAR119	42.872949	1.560063	680	209	5
	Enchantées	ASAR118	42.869721	1.563998	700	229	307
	Esplourgues	ASAR122	42.868193	1.562145	705	234	45
	Bédeilhac	ASAR117	42.871762	1.570543	710	239	988
	Bouicheta	ABOU103	42.870497	1.569947	780	315	178
	Moutons	ABOU104	42.86925	1.57210	850	385	30
Clot la Carbonnière	Monique	ASAR113	42.828093	1.622763	650	130	110
	Midi	ASAR114	42.829686	1.625618	705	185	170
Quié de Lujat	Souloumbrié	ASAR116	42.825914	1.678243	910	390	270
	Mirouge	ABOU102	42.80611	1.67556	1096	576	~10
Siech	Siech	ASAR112	42.882620	1.545914	676	70	1220
Roc de Trabinet	Herbo-Blanco	ASAR120	42.859829	1.525118	1115	425	65

Table 1. Locations of visited cavities, their elevations relative to the Ariège River and its tributaries (Vicdessos and Saurat), and their current lengths.

Sample	Mass (g)	[^{27}Al] (ppm)	[^{27}Al] × 10^{17} (at g^{-1})	Added spike (µL)	^{26}Al/^{27}Al (×10^{-14})
LO4	21.93	158.30±1.53	35.33±0.34	0	1.58±0.25
LO4b	23.96	13.98±0.09	3.12±0.02	251	2.61±0.32
LO4c	19.99	241.40±1.24	53.88±0.28	0	0.57±0.17

Table 2. Aluminum measurements testing the effect of residual muscovite on observed Al contents. The Al spike has an Al concentration of 9,372 ± 47 ppm.

Sample ID	Sample (lab ID)	Cave	Facies and lithologies	Relative elevation (m)	^{10}Be (10^3 at g^{-1})	^{26}Al (10^3 at g^{-1})	^{26}Al/^{10}Be	Burial duration (Ma)	Paleodenudation rate (mm kyr^{-1})
ASAR117_001	BE1	Bédeilhac - Vidal gallery	Sand, coarse to very coarse, may be pebbly	239	81±16	29±11	0.4±0.2	6.31±0.99	7±1
ASAR117_002	BE2	Bédeilhac - Main Gallery	Sand, coarse to very coarse	239	35±10	21±9	0.6±0.3	5.26±1.42	27±8
ASAR117_003	BE3	Bédeilhac - Tombeau de Rolland	Amalgamated granite pebbles	239	41±7	8±4	0.2±0.1	7.61±1.24	7±1
ABOU118_001	*CALA-14-01*	*Enchantées Cave*	*Medium to coarse sandstones*	*229*	*91±9*	*65±8*	*0.7±0.1*	*4.72±0.3*	*13±1*
ASAR118_001b	CALA-14-01b	Enchantées Cave	Medium to coarse sandstones	229	66±11	22±4	0.3±0.1	6.33±0.49	8±1
ABOU118_002	*CALA-14-02*	*Enchantées Cave*	*Medium to coarse yellow sandstones*	*229*	*61±4*	*82±20*	*1.3±0.3*	*3.47±0.55*	211±13
ABOU118_003	*CALA-14-03*	*Enchantées Cave*	*Medium to coarse sandstones*	*229*	*72±9*	*348±41*	*4.8±0.8*	*0.68±0.37*	*127±16*
ABOU120_001	CALA-14-04	Esplourgues Cave	Medium to coarse sandstones	234	29±5	37±17	1.3±0.6	3.70±1.32	443±71
ABOU120_002	*CALA-14-05*	*Esplourgues Cave*	*Medium to coarse sandstones*	*234*	*65±5*	*84±24*	*1.3±0.4*	*3.58±0.69*	199±16
ABOU119_001	CALA-14-06	Bédeilhac Quarry	Sand, coarse to locally loamy	209	70±7	59±20	0.8±0.3	4.5±0.87	20±2
ASAR110_001	LO1	Lombrives-Lions Gallery	Sand, medium to very coarse	114	21±6	41±21	1.9±1.1	2.83±1.6	147±42
ASAR110_002	LO2	Lombrives (F1)	Amalgamated granite pebbles	114	29±3	3±3	0.1±0.1	8.81±1.67	5±1
ASAR110_003	LO3	Lombrives - Vierge Gallery (F1)	Sandstones, medium to coarse	114	36±2	30±10	0.8±0.3	4.52±0.83	38±2

Sample ID	Sample (lab ID)	Cave	Facies and lithologies	Relative elevation (m)	^{10}Be (10^3 at g^{-1})	^{26}Al (10^3 at g^{-1})	^{26}Al/^{10}Be	Burial duration (Ma)	Paleodenudation rate (mm kyr^{-1})
ASAR110_004	LO4	Lombrives - Vierge Gallery (F1)	Sandstones, medium to coarse	114	45±2	56±9	1.3±0.2	3.57±0.37	49±2
ASAR110_004b	LO4b	Lombrives - Vierge Gallery (F1)	Amalgameted quartzite pebbles	114	50±2	69±9	1.4±0.2	3.34±0.3	49±2
ASAR110_005	LO5	Lombrives - Salines (F1)	Amalgamated granite pebbles	114	22±2	14±8	0.6±0.4	5.18±1.48	44±5
ASAR110_006	LO6	Lombrives (F1)	Amalgamated granite pebbles	114	38±4	11±7	0.3±0.2	6.91±1.49	11±1
ASAR110_007	LO7	Lombrives (F3)	Sandstones, fine to medium	114	23±2	14±5	0.6±0.2	5.33±1.03	39±3
ASAR110_008	LO8	Lombrives - Mamelle Gallery	Sands, fine	114	98±11	16±9	0.2±0.1	7.9±1.3	3±1
ASAR110_009	Lo12-01	Lombrives (F1)	Amalgamated granite pebbles	114	8±1	B.D.L.	B.D.L.	-	-
ASAR110_010	Lo12-02	Lombrives - Vierge Gallery	Sandstones, medium to coarse	114	33±2	42±21	1.3±0.6	3.79±1.42	60±3
ASAR111_001	LS1	Lombrives - Tunnel	Sandstones, medium	119	13±1	38±9	2.9±0.8	1.82±0.63	400±43
ABOU102_001	LUJ1	Mirouge cave	Medium to very coarse rubified sandstones	576	9±1	10±6	1.2±0.7	3.98±1.68	207±24
ABOU102_002	LUJ2	Mirouge cave	Medium to very coarse rubified sandstones	576	114±18	B.D.L.	B.D.L.	-	-
ABOU102_003	LUJ3	Mirouge cave	Medium to very coarse rubified sandstones	576	19±2	B.D.L.	B.D.L.	-	-
ABOU102_003b	LUJ3b	Mirouge cave	Medium to very coarse rubified sandstones	576	8±1	B.D.L.	B.D.L.	-	-

Sample ID	Sample (lab ID)	Cave	Facies and lithologies	Relative elevation (m)	^{10}Be (10^3 at g^{-1})	^{26}Al (10^3 at g^{-1})	^{26}Al/^{10}Be	Burial duration (Ma)	Paleodenudation rate (mm kyr^{-1})
ABOU104_001	MOU1	Moutons Cave	Cemented medium to very coarse sands (yellow-ochre)	385	16±2	6±6	0.4±0.4	6.19±1.85	-
ASAR104_001b	MOU1b	Moutons Cave	Cemented medium to very coarse sands (yellow-ochre)	385	51±7	B.D.L.	B.D.L.	-	-
ASAR104_001c	MOU1c	Moutons Cave	Cemented medium to very coarse sands (yellow-ochre)	385	30±6	B.D.L.	B.D.L.	-	-
ABOU101_005	Ni-13-05	Niaux – Marbre Gallery (F2)	Amalgamated pebbles	142	55±3	26±9	0.5±0.2	5.74±0.91	797±101
ABOU101_008	*Ni-13-08*	*Niaux – Bison Rouge Gallery*	*Amalgamated medium to coarse sands & pebbles*	*142*	*27±3*	*16±12*	*0.6±0.5*	*5.32±1.79*	13±1
ABOU101_010	*Ni-13-10*	*Niaux – Bison Rouge Gallery*	*Sandstones, medium to coarse*	*142*	*73±7*	*27±16*	*0.4±0.2*	*6.3±1.34*	480±62
ABOU101_012	Ni-13-12	Niaux – Éboulis Gallery	Amalgamated quarzite & granite pebbles	142	8±1	17±8	2.1±1.1	2.77±1.59	176±17
ABOU101_013	Ni-13-13	Niaux – Éboulis Gallery	Sands, medium to very coarse, may be pebbly	142	21±2	97±27	4.7±1.4	0.8±0.76	409±50
ABOU101_015	Ni-13-15	Niaux– Gallery of the counts of Foix (F3)	Amalgamated medium to coarse sands & gneiss pebbles	142	25±4	32±16	1.3±0.7	3.69±1.54	417±46
ABOU101_017	Ni-13-17	Niaux– Gallery of the counts of Foix (F1)	Amalgamated medium sands & pebbles (quartzites, granitoids)	142	B.D.L	24±24	-	-	-
ABOU101_020	Ni-13-20	Niaux– Gallery of the counts of Foix (F3)	Amalgamated quartzite & granitoid pebbles	142	29±4	104±28	3.6±1.1	1.37±0.7	522±87

Sample ID	Sample (lab ID)	Cave	Facies and lithologies	Relative elevation (m)	^{10}Be (10^3 at g^{-1})	^{26}Al (10^3 at g^{-1})	^{26}Al/^{10}Be	Burial duration (Ma)	Paleodenudation rate (mm kyr^{-1})
ABOU101_023	Ni-13-23	Niaux– Gallery of the counts of Foix (F3)	Medium to very coarse sandstones	142	28±3	53±19	1.9±0.7	2.84±0.98	447±55
ASAR101_001	Ni12-02	Niaux– Carrefour Cartailhac	Sand, medium to very coarse	142	19±3	10±6	0.5±0.3	5.69±1.59	456±40
ASAR103_002	*SED-13-02*	*Bouicheta Cave*	*Cemented medium to very coarse sands (yellow-ochre)*	*315*	*30±5*	*33±17*	*1.1±0.6*	*4.03±1.38*	39±7
ASAR116_001	SO1	Souloumbrié	Amalgamated smoky quartzite pebbles	460	16±7	B.D.L.	B.D.L.	-	427±78

Table 3. ^{10}Be and ^{26}Al concentrations, burial ages, and paleodenudation rates obtained for sampled caves. B.D.L., below detection limit. Burial durations were computed by solving Equation (3) with a Monte Carlo approach (Blard et al., 2019), assuming a mean watershed palaeoelevation of 1,990 m a.s.l. for the buried material (see Section 4.2.1). Derived maximum palaeodenudation rates were calculated from ^{10}Be concentrations (corrected for radioactive decay) using burial durations computed from the ^{26}Al/^{10}Be ratios and the production rates described in Section 4.2.1. Samples reported in italics contained residual muscovite, and the ^{26}Al concentrations reported for those samples may be inaccurate. F1, "Lombrives alluvial formation"; F3, "conglomerates of the gallery of the counts of Foix" (see Section 2.1). Additional data are available on supp. info. or on request.

Sample	Cave	Mass (mg)	T (°C) 20 min	^{20}Ne (10^{10} at g^{-1})	^{21}Ne/^{20}Ne (10^{-3})	^{22}Ne/^{20}Ne (10^{-1})	Cosmogenic ^{21}Ne^a (10^7 at g^{-1})	Cosmogenic ^{21}Ne^b (10^7 at g^{-1})
LO12-02	Lombrives	287.2	1446	1.89±0.07	3.58±0.06	1.056±0.011	1.28±0.27	0.86±0.37
LUJ1	Mirouge	304.9	1446	1.38±0.05	4.49±0.09	1.004±0.013	2.20±0.26	1.78±0.36
SO1	Souloumbrié	228.4	500	0.99±0.037	3.19±0.07	1.013±0.007	0.29±0.14	-
			1300	0.46±0.017	5.27±0.15	1.034±0.015	1.09±0.11	-

Sample	Cave	Mass (mg)	T (°C) 20 min	^{20}Ne (10^{10} at g^{-1})	$^{21}Ne/^{20}Ne$ (10^{-3})	$^{22}Ne/^{20}Ne$ (10^{-1})	Cosmogenic $^{21}Ne^{a}$ (10^{7} at g^{-1})	Cosmogenic $^{21}Ne^{b}$ (10^{7} at g^{-1})
						Total	1.38±0.18	0.96±0.31
MOU1	Moutons	272.7	1400	1.36±0.05	3.78 0.05	1.033±0.01	1.20±0.19	0.78±0.31
CALA-14-01b	Enchantées	250.8	1400	1.32±0.045	3.83 0.06	1.06±0.011	1.22±0.19	0.80±0.31
BE1	Bédeilhac	201.7	1400	1.18±0.04	4.02 0.09	1.013±0.012	1.32±0.19	0.90±0.32

Table 4. Neon isotopic data from the sampled caves. All samples were analyzed with the Helix SFT, except SO1, which was measured with the Helix MC.
[a] Cosmogenic ^{21}Ne excess calculated using Equation (5) following Honda et al. (2015).
[b] Cosmogenic ^{21}Ne corrected for a maximum potential nucleogenic ^{21}Ne build-up of $(4.2 \pm 2.5) \times 10^{6}$ at g^{-1} (see Section 5.2).

Sample	Cave	Altitude (m)	^{10}Be (10^{3} at g^{-1})	^{21}Ne (10^{7} at g^{-1})	$^{21}Ne/^{10}Be$	Burial duration (Ma)	Corrected burial duration[#] (Ma)	Paleodenudation rate (mm kyr^{-1})
LO12-02	Lombrives	114	33±2	1.28±0.27	393±84	9.0±0.4	7.8±0.8	4.5±0.2
LUJ1	Mirouge	576	9±1	2.20±0.26	2563±423	12.6±0.3	10.4±0.4	2.8±0.3
SO1	Souloumbrié	460	16±7	1.38±0.18	870±376	10.6±0.9	9.1±1.0	4.2±1.7
MOU1	Moutons	385	16±2	1.20±0.19	743±148	10.3±0.4	9.0±0.8	4.8±0.6
CALA-14-01b	Enchantées	229	91±9	1.22±0.19	134±25	6.8±0.3	5.5±0.8	4.7±0.5
BE1	Bédeilhac	239	81±16	1.32±0.19	163±40	7.2±0.5	5.9±0.8	4.4±0.8

Table 5. $^{10}Be/^{21}Ne$ burial durations and palaeodenudation rates calculated using Equation (4) and a watershed palaeoelevation of 1,990 m a.s.l. Palaeodenudation rates were computed from the ^{10}Be concentrations corrected for radioactive decay since burial.

[#] Burial durations computed after correcting the cosmogenic ^{21}Ne concentration for a maximum nucleogenic contribution of $(4.2 \pm 2.5) \times 10^{6}$ at g^{-1}.